

The signals of doomsday II: Cosmological signatures of late time $SU(3)_c$ symmetry breaking

Amartya Sengupta,^{a,b} Dejan Stojkovic,^a L.C.R. Wijewardhana^b

^a*HEPCOS, Department of Physics, SUNY at Buffalo, Buffalo, NY 14260-1500, USA*

^b*Department of Physics, University of Cincinnati, Cincinnati, Ohio 45221, USA*

E-mail: amartyas@buffalo.edu, ds77@buffalo.edu,
rohana.wijewardhana@gmail.com

ABSTRACT: The only two gauge symmetries which remain unbroken today are $SU(3)_c$ and $U(1)_{EM}$. Both are crucial for our universe to appear the way it does and for our form of life to exist. Unless we are very special observers living at the very end of the cosmological symmetry-breaking chain, there is no reason to believe that these two symmetries will remain unbroken forever. In this paper, we investigate the cosmological observational signatures of a late-time $SU(3)_c$ symmetry breaking. We introduce a model with a new colored scalar field whose potential supports a first-order phase transition through nucleation of true-vacuum bubbles. We first calculate particle production due to vacuum mismatch across the expanding bubble wall, including both the scalar and the massive-gluon sectors. We then study the decays of the physical color-octet scalar and the massive gluons, and use `Pythia` to hadronize their decay products and determine the resulting photon and neutrino spectra. We further include frictional effects from the ambient medium, which slow the bubble wall to a subluminal terminal velocity and thereby open the possibility of an observable signal reaching us before the wall itself. In addition to the direct vacuum-mismatch contribution, we analyze thermal particle production sourced by frictional energy dissipation into the shocked medium and show that, for the benchmark scenarios considered here, this thermal channel can dominate by many orders of magnitude. The resulting high-energy photon and neutrino spectra constitute a long-range observational signature which, if ever observed, could be interpreted as a signal of cosmic doomsday.

Contents

1	Introduction	1
2	Model for $SU(3)_c$ gauge symmetry breaking	2
3	Propagation of the true vacuum bubble	6
4	Particle production due to vacuum mismatch	6
5	Overview of TeV-Scale color states	9
5.1	Phenomenology of the color-octet scalar G_H	11
5.1.1	Hadronization and final-state yields for the color octet	12
5.2	Phenomenology of a massive gluon	14
5.2.1	Branching ratio and decay width at $M_g \sim 1$ TeV.	16
5.2.2	Hadronization and final-state yields	16
6	Relativistic bubble–wall dynamics in a viscous medium and terminal velocity	17
6.1	Equation of motion and terminal balance	17
6.2	Proper–time formulation	18
6.3	Evolution of the proper acceleration and approach to terminal motion	19
7	Particle production with frictional effects due to vacuum mismatch	19
8	Thermal particle production from frictional dissipation in the $SU(3)_c$ transition	21
8.1	Thermal particle production in the scalar and gluon channels	24
8.2	Thermal spectra for the scalar and gluon sectors	28
9	Photon or neutrino signal lead time	30
10	Conclusions	32
A	Appendix A: Symmetry breaking patterns from the adjoint potential	33
B	Appendix B: Quartic trace identity for $SU(3)$ adjoint fields	37
C	Appendix C: Particle production from a massive vector field	38
D	Appendix D: Derivation of $\Gamma(G \rightarrow q\bar{q})$	40
E	Appendix E: Derivation of $\Gamma(G_H \rightarrow q\bar{q})$	42
F	Appendix F: Derivation of $\Gamma(G_H \rightarrow gg)$	44

G	Appendix G: Justification of the cutoffs for vacuum–mismatch and thermal production in the $SU(3)_c$ transition	46
H	Appendix H: Proper Acceleration of the Bubble Wall	48
I	Appendix I: Numerical procedure	49

Contents

1 Introduction

It is believed that our universe in its history went through a series of phase transitions in which an original gauge symmetry group went broken either completely or down to a smaller subgroup. These processes can be considered violent since the whole structure of the universe gets rearranged, and the resulting new phase in the universe does not resemble much the previous one. The only two gauge symmetries that remain unbroken today are $SU(3)_c$ and $U(1)_{EM}$. However, there is no reason to believe that they will remain unbroken forever. Once they break, the universe will rearrange again, which will have very dramatic consequences for all the life forms in it, including ours. For example, if $SU(3)_c$ symmetry breaks, the gluons will become massive, and quarks will no longer be confined inside the protons and neutrons any more (except perhaps if one of the subgroups remains unbroken and thus the corresponding gluons remain massless). It is hard to imagine what the universe will look like in this new phase, but it is certain that it will not be able to support a life similar to ours. Even if such a possibility is very remote, the seriousness of its consequences warrants a detailed study of the signature of such a phase transition. The purpose of this paper is to study the astrophysical signature of the late time $SU(3)_c$ symmetry breaking (the signature of $U(1)_{EM}$ symmetry breaking will be studied elsewhere).

We will first write down the model supporting $SU(3)_c$ gauge symmetry breaking, which is still consistent with the current observational data. To avoid most of the astrophysical and collider constraints, we will consider a first-order phase transition. Such a model inevitably contains a new massive colored scalar field responsible for the symmetry breaking. We will then derive the dynamics of a true vacuum bubble propagation and particle production in its background. Since the vacuum state of the fields is changing during the bubble propagation in space, the process will result in a copious particle production due to the vacuum mismatch. Eventually, we are interested in the long-range observable signature detectable on Earth. We will therefore first calculate the decay of the massive colored scalar field and massive gluons. We will then use `Pythia 8` to hadronize the decay products and finally calculate their decays into photons and neutrinos. In addition, we will analyze the phenomenology of the physical color-octet scalar and of the massive gluons in the broken phase, including their decay widths, branching ratios, and the corresponding photon and neutrino yields. We will also show that, besides the direct vacuum-mismatch contribution, frictional dissipation

of the bubble-wall energy into the shocked medium can generate an additional thermal population of heavy quanta whose contribution may dominate the final signal by many orders of magnitude.

If the propagation of the bubble wall is slowed down due to interaction with surrounding matter and radiation, we will be able to detect these photons and neutrinos before the bubble wall hits us. To take into account this friction, we derive the dynamics of the wall in a viscous medium and find the time-dependent proper acceleration which drives the particle production. Once the terminal velocity is reached and the proper acceleration drops to zero, particle production due to this mechanism also stops. Thus, we will also show neutrino and photon spectra produced only up to the moment when the terminal velocity is reached. We will further show that the same friction responsible for slowing the wall also deposits a substantial amount of energy into the surrounding medium, leading to thermal particle production behind the wall. This thermal component persists even after the direct acceleration-driven vacuum-mismatch contribution becomes strongly suppressed, and therefore provides an additional and potentially dominant source of observable high-energy photons and neutrinos.

2 Model for $SU(3)_c$ gauge symmetry breaking

When considering a model for $SU(3)_c$ gauge symmetry breaking, we have two options: either a first- or second-order phase transition. A second-order phase transition is a smooth process in which the field responsible for the symmetry breaking is smoothly rolling down its own potential. If we are interested in the late-time phase transition, such a field must be very light, i.e. with a mass of the order of the current temperature in the universe ($\sim 10^{-4}\text{eV}$). Such a field will be very difficult to hide from the current collider constraints. We therefore choose to study a first-order phase transition involving a colored scalar field with a mass above the current collider limits. In this scenario, we live in the false vacuum where $SU(3)_c$ gauge symmetry is not broken. Eventually we will tunnel into the true vacuum, however, if the lifetime of the false vacuum is longer than the age of the universe, no observational constraints (either cosmological, or collider) will be violated. Although observational constraints indicate that most of our universe is currently in the unbroken phase, they do not exclude the possibility that bubbles of the true vacuum already exist within our universe.

Consider a Lagrangian density that is invariant under $SU(3)_c$ transformations:

$$\mathcal{L} = -\frac{1}{2}\text{Tr}F_{\mu\nu}F^{\mu\nu} + \frac{1}{2}\text{Tr}(D_\mu\Phi)(D^\mu\Phi) - V(\Phi), \quad (2.1)$$

where the field strength and covariant derivative are

$$F_{\mu\nu} = \partial_\mu A_\nu - \partial_\nu A_\mu + ig[A_\mu, A_\nu], \quad D_\mu\Phi = \partial_\mu\Phi + ig[A_\mu, \Phi], \quad A_\mu = A_\mu^a T^a, \quad (2.2)$$

where $\mu, \nu = 0, 1, 2, 3$, and repeated indices are summed with the Minkowski metric $\eta^{\mu\nu}$. The scalar field Φ is taken to be in the adjoint representation of $SU(3)_c$. $D^\mu\Phi$ represents the covariant derivative of Φ , and g is the gauge coupling constant.

Varying Φ leads to the equation of motion

$$D_\mu D^\mu \Phi = \frac{\partial V}{\partial \Phi}. \quad (2.3)$$

The expanded form of the covariant derivative acting on Φ is therefore

$$D_\mu D^\mu \Phi = \eta^{\mu\nu} D_\mu D_\nu \Phi = \eta^{\mu\nu} \left[\partial_\mu \partial_\nu \Phi + i g \left([\partial_\mu A_\nu, \Phi] + 2 [A_\mu, \partial_\nu \Phi] \right) - g^2 [A_\mu, [A_\nu, \Phi]] \right]. \quad (2.4)$$

The potential is given by

$$V(\Phi) = \frac{\mu^2}{4} (\text{Tr} \Phi^2) + \frac{\lambda_1}{16} (\text{Tr} \Phi^2)^2 + \frac{\lambda_2}{6} (\text{Tr} \Phi^3) + V_0. \quad (2.5)$$

We assume the breaking pattern $SU(3)_c \rightarrow U(2)$, which leaves four scalars massless and gives mass to the remaining four. A detailed classification of the vacuum alignments and the corresponding unbroken subgroups that can arise from this potential is presented in Appendix A, where we summarize the possible symmetry-breaking patterns of $SU(3)_c$. We require the potential to be bounded from below and set $\lambda_1 > 0$. The term $\text{Tr} \Phi^4$ is not included since it shares the structure of $(\text{Tr} \Phi^2)^2$ and therefore will not affect the qualitative outcomes (see Appendix B). A similar model was previously studied (see [1, 2]). The constant term V_0 serves merely as an overall shift in the potential, and for our purpose here can be set to zero.

In a convenient diagonal representation, Φ is Hermitian and traceless. This representation involves three real fields ψ_1 , ψ_2 , and $\psi_3 = -(\psi_1 + \psi_2)$. Minimizing $V(\Phi)$ leads to the relation

$$\psi_1 = \psi_2 = -\frac{\psi_3}{2} \equiv \psi, \quad (2.6)$$

corresponding to the $SU(3)_c \rightarrow U(2)$ breaking direction. There are in total eight real scalar degrees of freedom in the adjoint of $SU(3)_c$. After the breaking $SU(3)_c \rightarrow U(2)$, four colored Goldstone modes are eaten by the four massive gluons, leaving four physical scalar degrees of freedom. For simplicity, we write the potential below for a single scalar component associated with the diagonal generator T_j .

Expressing the potential as a function of ψ yields

$$V(\psi) = \frac{3}{2} \mu^2 \psi^2 + \frac{9}{4} \lambda_1 \psi^4 - \lambda_2 \psi^3 + V_0. \quad (2.7)$$

Introducing new definitions

$$\psi_0 \equiv \frac{2 \lambda_2}{9 \lambda_1}, \quad \epsilon_0 \equiv \lambda_1 - \frac{2 \mu^2}{3 \psi_0^2}, \quad (2.8)$$

allows a more convenient rewriting of the potential

$$V(\psi) = \frac{9}{4} \lambda_1 \psi^2 (\psi - \psi_0)^2 - \frac{9}{4} \epsilon_0 \psi_0^2 \psi^2 + V_0. \quad (2.9)$$

The parameter ϵ_0 represents the degree of the fine-tuning in $V(\psi)$. If $\epsilon_0 = 0$, the potential has two degenerate minima at $\psi = 0$ and $\psi = \psi_0$, and the fine-tuning is absent.

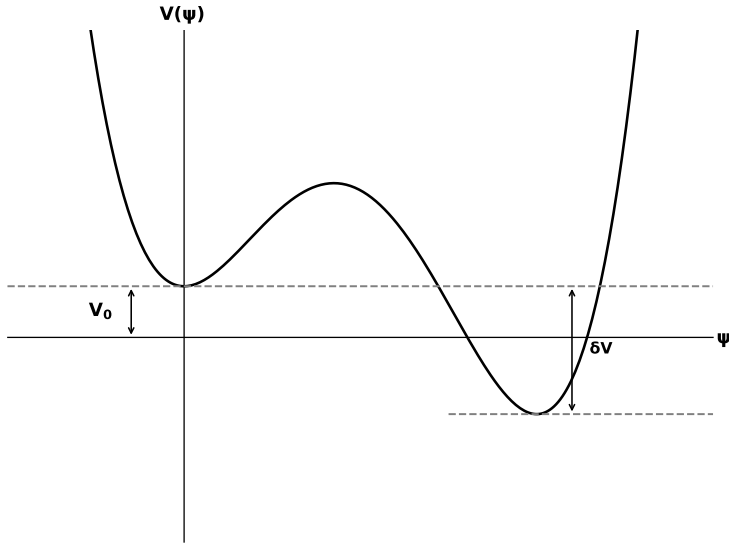


Figure 1. Characteristic potential for a first order phase transition. There exist the false vacuum where the symmetry is unbroken, $\psi = 0$, and the true vacuum where the symmetry is broken, $\psi \neq 0$. δV is the difference in energy densities between the vacua. V_0 is the overall shift of the potential.

For a small and positive ϵ_0 , the global minimum shifts slightly to $\psi = \psi_0(1 + \epsilon_0/\lambda_1)$. Expanding about the shifted minimum $\psi = \psi_0(1 + \epsilon_0/\lambda_1)$, one finds at leading order in ϵ_0 , the difference in energy densities between these two vacua is

$$\delta V \simeq \frac{9}{4}\epsilon_0\psi_0^4. \quad (2.10)$$

Figure 1 illustrates the characteristic potential for this first-order phase transition scenario. It shows the false vacuum with unbroken symmetry at $\psi = 0$ and the true vacuum with broken symmetry at $\psi \neq 0$. The difference in energy density between these vacua is denoted by δV , while V_0 is the overall shift of the potential that our calculations do not depend on. But for example, we could use this freedom to shift the whole potential up to avoid tunneling into an AdS space with negative cosmological constant (where the whole region would collapse into a black hole).

The presence of a deeper true minimum in the potential indicates that any location in the universe will ultimately tunnel into the true vacuum, where the $SU(3)_c$ symmetry is broken. However, the rate of tunneling is determined by the energy difference between the vacua and the height of the potential barrier. For a phenomenologically valid model, the tunneling rate must be sufficiently slow so that the lifetime of the false vacuum is at least of the order of the age of the universe.

In the false vacuum state, where $\psi = 0$, excitations of the new colored scalar field have a mass scale $m_\psi \sim \mu$. A natural choice for μ is around $\mathcal{O}(1\text{TeV})$, aligning with the anticipated scale for new physics beyond the Standard Model. Moreover, it would be challenging to hide a colored scalar field significantly lighter than this scale. Selecting this scale naturally avoids all the experimental constraints from QCD.

Next, we examine the constraints on the parameter ϵ_0 . A crucial question is how long the universe could exist in the supercooled false vacuum state $\psi = 0$. Transitioning from this false to the true vacuum occurs through bubble nucleation of the true vacuum within the false vacuum. Within the semi-classical approximation, the transition probability per unit space-time volume is given by

$$\Gamma = B e^{-S_E}, \quad (2.11)$$

where S_E is the Euclidean action of the $O(4)$ -symmetric bounce solution describing tunneling, and B is a constant of order $\mathcal{O}(\text{TeV}^4)$. Since we only consider the magnitude of the transition rate, we neglect the constant B . To compute S_E , we use the standard method defined in [3].

At zeroth order in ϵ_0 , the one-dimensional Euclidean action per unit volume for tunneling is

$$S_1 = \int_0^{\psi_0} d\psi' \sqrt{2V(\psi')} \approx \sqrt{\frac{\lambda_1}{8}} \psi_0^3. \quad (2.12)$$

In the thin-wall approximation and zero-temperature limit, the radius of the critical bubble is given by

$$R_0 = \frac{3S_1}{\delta V} = \frac{\sqrt{2\lambda_1}}{3} \frac{1}{\epsilon_0 \psi_0}. \quad (2.13)$$

The Euclidean action for an $O(4)$ -symmetric bubble is:

$$S_E = -\frac{1}{2} \delta V \pi^2 R_0^4 + 2\pi^2 R_0^3 S_1 = \frac{\pi^2 \lambda_1^2}{54} \frac{1}{\epsilon_0^3}. \quad (2.14)$$

The decay rate per unit volume and time is defined in (2.11). We require that our observable universe, with a four-volume of the order of t_{Hubble}^4 , remains in the unbroken phase (i.e. false vacuum). This requirement corresponds to $\Gamma t_{\text{Hubble}}^4 \lesssim 1$. With $t_{\text{Hubble}} \sim 10^{10}$ years, this implies the limit $S_E > 400$. For a generic value $\lambda_1 \sim 1$, vacuum stability imposes only a mild fine-tuning condition, $\epsilon \lesssim 0.1$. Furthermore, $\epsilon_0 \lesssim 0.1$ is also sufficient to validate the thin-wall approximation. For this study, we adopt the benchmark values $\epsilon_0 = 0.076$ and $\lambda_1 = 1$, with a true vacuum expectation value of $\psi = 1058$ GeV. These choices yield $\psi_0 = 983.3$ GeV, surface tension $S_1 = 3.36 \times 10^8$ GeV³, vacuum energy difference $\Delta V = 1.60 \times 10^{11}$ GeV⁴, and a critical bubble radius $R_0 = 6.31 \times 10^{-3}$ GeV⁻¹. The corresponding bounce action is $S_E \simeq 416$.

Evaluating the decay probability, we obtain

$$\Gamma t_{\text{Hubble}}^4 (B = (1 \text{ TeV})^4) = 7.96 \times 10^{-3}, \quad (2.15)$$

well below unity. With our chosen parameters corresponding to an $SU(3)_c$ breaking scale approximately of order 1 TeV, this represents the closest value attainable to unity within the phenomenologically allowed region of parameter space. This corresponds to a tunneling rate

$$\Gamma \simeq 1.6 \times 10^{-128} \text{ GeV}^4, \quad (2.16)$$

which ensures that the false vacuum at $\psi = 0$ is cosmologically long-lived. Thus, the $SU(3)_c$ false vacuum is metastable on Hubble timescales, satisfying the stability criterion $\Gamma t_{\text{Hubble}}^4 \lesssim 1$ (see Section 4).

3 Propagation of the true vacuum bubble

When the scalar field tunnels through the potential barrier, a bubble of true vacuum forms and begins to expand [3–5]. To get the dynamics of the bubble, we neglect the interactions between Φ and other fields (e.g. fermions, gauge fields, etc.). The dynamics of the scalar field, $\Phi(\rho)$, is then given by the action

$$S(\Phi) = \int d^4x \left(\frac{1}{2} (\partial_\mu \Phi)^2 - V(\Phi) \right), \quad (3.1)$$

yielding the classical equation of motion

$$-\partial_t^2 \Phi + \nabla^2 \Phi - V'(\Phi) = 0. \quad (3.2)$$

Upon Wick rotation, $t \rightarrow i\tilde{\tau}$, we obtain the following

$$\partial_{\tilde{\tau}}^2 \Phi + \nabla^2 \Phi - V'(\Phi) = 0. \quad (3.3)$$

Considering a $O(4)$ symmetric bounce solution, the equation further simplifies to

$$\frac{d^2 \Phi}{d\rho^2} + \frac{3}{\rho} \frac{d\Phi}{d\rho} = V'(\Phi), \quad (3.4)$$

with $\rho = \sqrt{\tilde{\tau}^2 + r^2}$, indicating dependence only on ρ . The bounce solution satisfying the boundary conditions at nucleation ($t = 0$) is

$$\Phi(t, \vec{x}) = \Phi(\rho = \sqrt{r^2 - t^2}). \quad (3.5)$$

Here, the bubble contracts for $t < 0$, bounces at $t = 0$, and expands afterward. As usual, we cut the solution at $t = 0$ and consider only the expansion. Utilizing the thin-wall approximation, we express the scalar-field configuration as

$$\Phi(\rho) = \begin{cases} v, & \rho > R, \\ v_1, & \rho < R, \end{cases} \quad (3.6)$$

where v and v_1 represent the scalar field expectation values in false and true vacua, respectively, while R is the radius of the bubble.

Particle production during first-order phase transitions has been extensively studied in the literature (e.g., [5–48]). For our purposes, we begin by employing the vacuum-mismatch method, following Refs. [17, 49], and later discuss the thermal production mechanism generated by frictional dissipation in the medium behind the shock wall.

4 Particle production due to vacuum mismatch

The difference between the false and true vacua typically leads to particle creation. Outside, the bubble remains the false vacuum, while inside the field transitions to the true vacuum via

tunneling. This transition initiates the generation of massive scalar particles. By separating the scalar field into background and fluctuations, $\Phi = \Phi_c + h$, the fluctuation field h obeys

$$\partial_{\tilde{\tau}}^2 h + \nabla^2 h - V''(\Phi_c)h = 0. \quad (4.1)$$

Neglecting additional field interactions, this equation approximates as

$$\partial_{\tilde{\tau}}^2 h + \nabla^2 h - M^2 h = 0, \quad \tilde{\tau} < \tilde{\tau}^*, \quad (4.2)$$

$$\partial_{\tilde{\tau}}^2 h + \nabla^2 h - \mu^2 h = 0, \quad \tilde{\tau} > \tilde{\tau}^*, \quad (4.3)$$

where $\tilde{\tau}^*$ is the characteristic (Euclidean) time scale for the duration of the phase transition. We take here $\tilde{\tau}^* = -R_0$, where R_0 is the size of the bubble at the time of nucleation. The reason for this is that the bubble propagation is a motion with a constant proper (in contrast to coordinate) acceleration. From the equation of motion $r^2 - t^2 = R_0^2$, one can derive the magnitude of the proper acceleration as $a = 1/R_0$ (see appendix). Thus, the process of particle creation in this context admits an Unruh-like interpretation, in which the amount of radiation is determined by the proper acceleration. Since in the absence of friction this acceleration is constant during the bubble expansion, particles are produced continuously as the bubble expands. We also note that the proper acceleration is defined in terms of the proper time of an observer who is momentarily at rest with respect to the bubble wall, and it is not equal to a coordinate acceleration measured by a distant observer (which actually goes to zero as the bubble wall approaches the speed of light).

The solution for h can be written as a combination of mode functions g_k , which satisfy $\nabla^2 g_k = -k^2$

$$g_k = \begin{cases} e^{\omega_- \tilde{\tau}} e^{i\vec{k} \cdot \vec{x}} & , \text{ for } \tilde{\tau} < \tilde{\tau}^* \\ A_k e^{\omega_+ \tilde{\tau}} e^{i\vec{k} \cdot \vec{x}} + B_k e^{-\omega_+ \tilde{\tau}} e^{i\vec{k} \cdot \vec{x}} & , \text{ for } \tilde{\tau} > \tilde{\tau}^* \end{cases} \quad (4.4)$$

For the scalar channel we use $\omega_+ = \mu_s$ in the true vacuum and $\omega_- = M_s$ in the false vacuum, while for the massive-gluon channel we use $\omega_+ = \mu_g$ in the true vacuum and $\omega_- = 0$ in the false vacuum. Concretely, the scalar mass in the false vacuum region is

$$M^2 = \frac{9}{2} \psi_0^2 [\lambda_1 - \epsilon_0], \quad (4.5)$$

while in the true vacuum region is

$$\mu^2 = \frac{9}{2} \psi_0^2 \left[\lambda_1 + 5\epsilon_0 + 6 \frac{\epsilon_0^2}{\lambda_1} \right]. \quad (4.6)$$

Since g_k and $\partial_{\tilde{\tau}} g_k$ must be continuous at $\tilde{\tau} = \tilde{\tau}^*$, for A_k and B_k we get

$$A_k = \frac{1}{2\omega_+} (\omega_+ + \omega_-) e^{-(\omega_+ - \omega_-)\tilde{\tau}^*} \quad (4.7)$$

$$B_k = \frac{1}{2\omega_+} (\omega_+ - \omega_-) e^{(\omega_+ + \omega_-)\tilde{\tau}^*}. \quad (4.8)$$

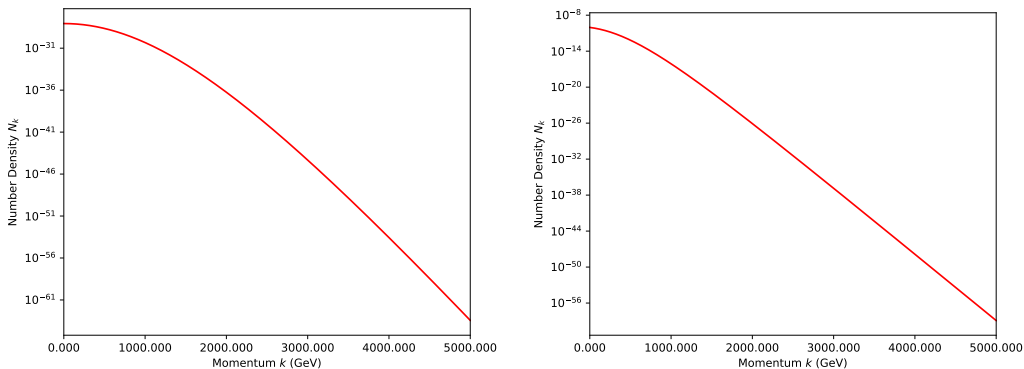


Figure 2. On the left we have number density N_k of the scalar colored particles and on the right we have number density N_k of the massive gluons created as a function of their momenta due to the vacuum mismatch

As explained above, we set $\tilde{\tau}^* = -R_0$. The particle creation spectrum is obtained from the Bogoliubov transform [49]

$$N_k = \frac{B_k^2}{A_k^2 - B_k^2} = \left[\frac{(\omega_+ + \omega_-)^2}{(\omega_+ - \omega_-)^2} e^{4\omega_+ R_0} - 1 \right]^{-1}. \quad (4.9)$$

The left-hand side of Figure 2 presents the momentum-dependent particle number density $N_k = \frac{dN}{dV d^3k}$ for the scalar field Φ . For our chosen parameters discussed previously, i.e. $\epsilon_0 = 0.076$, $\lambda_1 = 1$, we get the scalar mass in the false vacuum to be $M = 2000$ GeV, the bubble radius at the moment of nucleation is $R_0 \approx 6.3 \text{ TeV}^{-1}$, while the scalar mass in the true vacuum is $\mu \sim 2500$ GeV for the true vacuum located at 1058 GeV. The large vacuum pressure released during bubble expansion ($\Delta V \sim 0.16 \text{ TeV}^4$) provides the main energy source for producing massive particles in the true vacuum phase. The details of this production mechanism will be discussed later.

In models of this type, where the QCD gauge symmetry $SU(3)_c$ is broken by an adjoint scalar at the TeV scale, the residual unbroken subgroup is generically $U(2)$ (see Appendix B). In this vacuum alignment four gluons remain massless while the other four acquire masses of order $m_g = g_s \psi_0$, with ψ_0 the scalar expectation value. Adopting unitary (Proca) gauge, the massive gluons absorb the corresponding colored Goldstone modes and propagate as massive vectors.

The analysis of gluon production at zero comoving momentum requires additional care. Inside the broken phase, four of the eight gluons acquire mass, behaving as massive Proca fields with two transverse and one longitudinal polarization each, while the remaining four gluons stay massless. Before symmetry breaking, however, only the two transverse gluonic degrees of freedom are present as physical propagating modes; the longitudinal polarization emerges only after the vacuum expectation value of the adjoint scalar is established, when the corresponding colored Goldstones are absorbed. This distinction has important consequences for the mode matching at the bubble wall.

For the *transverse* polarizations, the matching proceeds in a close analogy with the photon calculation. At $k = 0$, one has $\omega_- = |k| = 0$ in the false vacuum and $\omega_+ = \sqrt{k^2 + m_g^2} = m_g$ in the true vacuum. The Bogoliubov transformation then gives

$$N_{k=0}^{(T)} = \left[e^{4m_g R_0} - 1 \right]^{-1}, \quad (4.10)$$

which is well defined for each transverse polarization. Including the multiplicity of the four massive gluons, each with two transverse polarizations, the transverse-only contribution to the gluon number density becomes

$$n_{\text{gluon}}(k=0) = 8 N_{k=0}^{(T)} = \frac{8}{e^{4m_g R_0} - 1}. \quad (4.11)$$

The *longitudinal* gluon polarization, in contrast, cannot be captured by this simple quench calculation. Since it is absent before the symmetry is broken, one cannot directly apply the two-oscillator matching used for the transverse modes. A correct treatment requires setting up the coupled system of the gauge bosons and the colored Goldstone fields, (G_μ^a, π^a) , and working in a covariant gauge such as R_ξ . The relevant gauge-invariant combinations, e.g.

$$\partial_\mu \pi^a - g_s v_c G_\mu^a, \quad (4.12)$$

must then be matched consistently across the wall. The resulting Bogoliubov coefficients for the longitudinal modes are in general different from those of the transverse ones, and will depend sensitively on the details of the scalar sector and the choice of gauge fixing. A full computation of this coupled scalar–vector dynamics is beyond the scope of the present analysis and will be developed in future work. For the purposes of the present phenomenological study, we therefore adopt the conservative choice of retaining only the transverse polarizations when quoting gluon production rates and spectra.

We emphasize that this estimate undercounts the full gluonic production, since the longitudinal polarizations of the massive gluons are omitted. However, this omission does not qualitatively affect our cosmological conclusions, since including the longitudinal modes would change the total massive-gluon multiplicity only by an $\mathcal{O}(1)$ factor rather than by an order of magnitude, and is therefore negligible on the logarithmic scales relevant for the present signal estimates. Nevertheless, adopting the transverse-only contribution provides a conservative lower bound on the gluon yield relevant for the present phenomenological study. The corresponding spectra are shown in the right-hand panel of Fig. 2, and the derivation of the transverse mode functions used in this expression is summarized in Appendix C.

5 Overview of TeV-Scale color states

In addition to the colored scalar field, Φ , once the symmetry is broken to $U(2)$ there emerge both massive and massless gluons. The four massive gluons behave analogously to the W bosons in $SU(2)$: they acquire mass through the breaking and do not form glueballs. However, they can form bound states through the residual gauge force mediated by the unbroken gauge bosons, much like the W^+ and W^- in the Standard Model can form a

bound state via their mutual Coulomb interaction. These massive-gluon bound states are expected to have masses in the multi-TeV range—approximately the sum of the constituent masses—and sizes set by Λ_{QCD} , analogous to charmonium ($c\bar{c}$) or bottomonium ($b\bar{b}$) systems.

The remaining four massless gluons correspond to the unbroken group and are expected to confine into ordinary glueballs with masses comparable to those of QCD. We do not further analyze the decay of the massive-gluon bound state, since its final-state signatures would be indistinguishable from those of the massive gluon decays. Mixed bound states of one scalar and a quark ($8 \times 3 \times \bar{3} \rightarrow 1$) carry an integer electric charge, while scalars in higher $SU(3)_c$ representations (3, 6, 10, 15, 21) can even form exotic fractionally charged hadrons. Although our analysis is primarily cosmological, we note that the benchmark mass scales we consider for the adjoint scalar and color-octet are consistent with current collider limits. In particular, the CMS search for four jet resonances at $\sqrt{s} = 13$ TeV [50] and the corresponding ATLAS analysis [51] and [52] place exclusion limits on new colored resonances ranging around 1.0 – 1.8 TeV scale. Our chosen benchmark points lie above these bounds, ensuring compatibility with existing collider constraints. In the following sections, we will detail the mass spectra, decay widths, and observational signatures of these TeV-scale colored states [53–58].

All spectra were generated with `Pythia 8 (v8.313)` [59, 60] using a fixed random seed and the Monash 2013 tune. To isolate the intrinsic particle-physics yields from model parameters and avoid dependence on collider or PDF assumptions, the new states (massive gluon, color-octet scalar) were generated as resonances at rest with their target mass, fixed width, and benchmark branching fractions. Parton showering, hadronization, and all weak/FSR decays were enabled, and long-lived mesons and muons were forced to decay so that neutrino and photon yields are fully captured. Each spectrum was produced with $\mathcal{O}(10^4)$ simulated decays, histogrammed in 1 GeV bins up to several TeV, and written to CSV. This procedure ensures that the photon and neutrino spectra shown in the figures represent the intrinsic decay yields of the TeV-scale colored states, independent of collider environments, while still incorporating the complete hadronization and decay chains.

Inside the bubble, in the new vacuum where the symmetry is broken, the field Φ (and also massive gluons) do not have to form color-free bound states and can freely propagate. However, outside of the bubble, in the false vacuum the symmetry is still unbroken, so colored excitations cannot remain free and must hadronize into $SU(3)_c$ singlets. Thus, if the bubble reaches the terminal velocity below the speed of light, for simplicity we assume that all the colored states whose ultimate decay products are to be observed on Earth, must first hadronize before decaying into photons and neutrinos.

When particles are produced at the boundary of an expanding bubble during a first-order phase transition, a subset of them will propagate outward into the false-vacuum region and another fraction will fall into the true-vacuum interior of the bubble. Those particles entering the true vacuum may themselves decay following the symmetries of the true vacuum, and in principle some of their lighter decay products could overtake the advancing bubble wall and reach the false-vacuum side; however, this fraction is extremely suppressed. In the present work, we focus exclusively on the population of particles that decay in the vicinity of the bubble wall and whose decay products propagate outward toward an observer located in

the false vacuum. The fraction of inward-going particles that later produce outward-moving decay products will be negligible, and thus we consistently ignore it in our analysis.

5.1 Phenomenology of the color-octet scalar G_H

In extensions of QCD with an adjoint scalar acquiring a TeV-scale VEV that we are considering here, the physical scalar octet G_H^a has mass (see Eq. 4.6)

$$M_{G_H} = 2.5 \text{ TeV}, \quad \text{for} \quad u = \langle \Phi \rangle = 1 \text{ TeV}. \quad (5.1)$$

We work in a traceless diagonal representation, which greatly simplifies the analysis by reducing the dynamics to a single scalar field that plays the role of the order parameter for the symmetry breaking. For this reason, the production formulas presented in the following are written for one representative physical scalar mode. However, in the full adjoint sector of $SU(3)_c$, there are eight real scalar components. After the breaking $SU(3)_c \rightarrow U(2)$, four of these are eaten by the four massive gluons, leaving four physical scalar degrees of freedom. Thus, the results shown here should be understood as applying to a single physical scalar mode. If the four physical scalars are approximately degenerate, the total scalar yield is obtained by multiplying the single-mode result by four. If their masses are split, as indicated for example in Eq. (2.28) of [2], the same analysis can be carried out for each mode separately with the appropriate mass inserted.

For the decay rate expressions of the physical color octet scalar we mostly followed [61–64] and the detail calculations are shown in Appendix E and F, while for the phenomenological aspects one can refer to [61, 62, 65–84]. In the present broken-color setup, the tree-level decay of a fixed adjoint component G_H^a into quark–antiquark pairs is most cleanly described by introducing an effective Yukawa interaction of the form

$$\mathcal{L}_{\text{int}} \supset -y_q \bar{q} T^a q G_H^a. \quad (5.2)$$

We treat this term as an effective phenomenological interaction that captures the decay of the physical scalar mode into quarks after symmetry breaking. Its microscopic origin is not specified in the present analysis, but it could naturally emerge in a suitable UV-complete extension.

For a single physical color-octet component, the corresponding tree-level partial width is then (see Appendix E)

$$\Gamma(G_H^a \rightarrow q\bar{q}) = \frac{y_q^2 M_{G_H}}{16\pi} \left(1 - \frac{4m_q^2}{M_{G_H}^2}\right)^{3/2}. \quad (5.3)$$

For the numerical benchmark below we adopt the phenomenological normalization

$$y_q = \eta_q \frac{m_q}{v}, \quad v = 246 \text{ GeV}, \quad (5.4)$$

and set $\eta_q = 1$ for all quark flavors. In this normalization, Eq. (5.3) becomes

$$\Gamma(G_H^a \rightarrow q\bar{q}) = \frac{\eta_q^2 m_q^2 M_{G_H}}{16\pi v^2} \left(1 - \frac{4m_q^2}{M_{G_H}^2}\right)^{3/2}. \quad (5.5)$$

The expression in Eq. (5.3) corresponds to the color trace of a fixed octet component, $\text{Tr}(T^a T^a) = T_R = \frac{1}{2}$.

For decays into gluons, the leading contribution arises at one loop through quark triangle diagrams. The corresponding partial width for a fixed adjoint component is (see Appendix F)

$$\Gamma(G_H^a \rightarrow gg) = \frac{5 \alpha_s^2 M_{G_H}^3}{6912 \pi^3} \left| \sum_q \frac{y_q}{m_q} F_{1/2}(\tau_q) \right|^2, \quad \tau_q \equiv \frac{4m_q^2}{M_{G_H}^2}, \quad (5.6)$$

where $F_{1/2}(\tau_q)$ is the standard spin- $\frac{1}{2}$ scalar loop form factor, given explicitly in Appendix F. With the same benchmark choice $y_q = \eta_q m_q/v$ and $\eta_q = 1$, this may be written as

$$\Gamma(G_H^a \rightarrow gg) = \frac{5 \alpha_s^2 M_{G_H}^3}{6912 \pi^3 v^2} \left| \sum_q \eta_q F_{1/2}(\tau_q) \right|^2. \quad (5.7)$$

Using $m_u = 2.2$ MeV, $m_d = 4.7$ MeV, $m_s = 96$ MeV, $m_c = 1.27$ GeV, $m_b = 4.18$ GeV, $m_t = 173$ GeV, and $\alpha_s = 0.09$, together with the benchmark choice $\eta_q = 1$, one finds the partial widths and branching ratios shown in Table 1.

Channel	Γ [GeV]	BR (%)
$u\bar{u}$	3.98×10^{-9}	< 0.01
$d\bar{d}$	1.82×10^{-8}	< 0.01
$s\bar{s}$	7.57×10^{-6}	< 0.01
$c\bar{c}$	1.33×10^{-3}	0.006
$b\bar{b}$	1.44×10^{-2}	0.060
$t\bar{t}$	2.39×10^1	99.921
gg	3.24×10^{-3}	0.014
Total	2.39×10^1	100

Table 1. Partial widths and branching fractions for a single physical color-octet component G_H^a ($M_{G_H} = 2.5$ TeV, $u = 1$ TeV) for the benchmark choice $y_q = m_q/v$.

The decay to $t\bar{t}$ overwhelmingly dominates (BR $\approx 99.9\%$) because the tree-level rate (5.3) scales as $(m_q/v)^2$, so the top channel benefits from the large top Yukawa coupling. Light-quark modes are suppressed by $(m_{u,d,s}/v)^2 \ll 10^{-6}$ and are therefore negligible. The loop-induced gg mode in Eq. (5.6) is suppressed by the one-loop factor and by the fermion-triangle form factor, and for the benchmark point considered here it remains subleading, with a branching fraction of order 0.01%.

5.1.1 Hadronization and final-state yields for the color octet

The partial width and BR of the decayed products were used as input to `Pythia 8` [59, 60]. Then `Pythia` performed the hadronization of the primary final state into jets of mesons and baryons and the decays of all unstable resonances into stable photons, leptons, and hadrons.

In these simulations, neutral mesons (e.g. $\pi^0 \rightarrow \gamma\gamma$) provide abundant high-energy photons, while charged mesons and heavy-flavor states decay semileptonically to neutrinos.

Photon and neutrino multiplicities for the color octet decay exceed those of other stable species by over an order of magnitude.

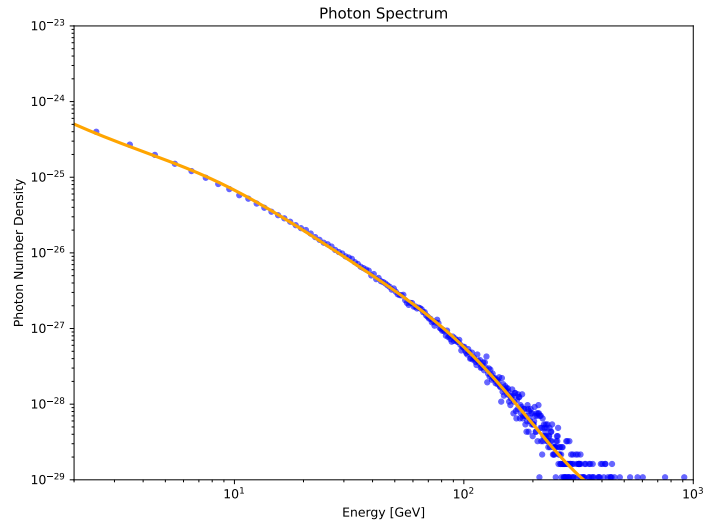


Figure 3. Differential energy spectrum of photons per 2.5 TeV color octet decay.

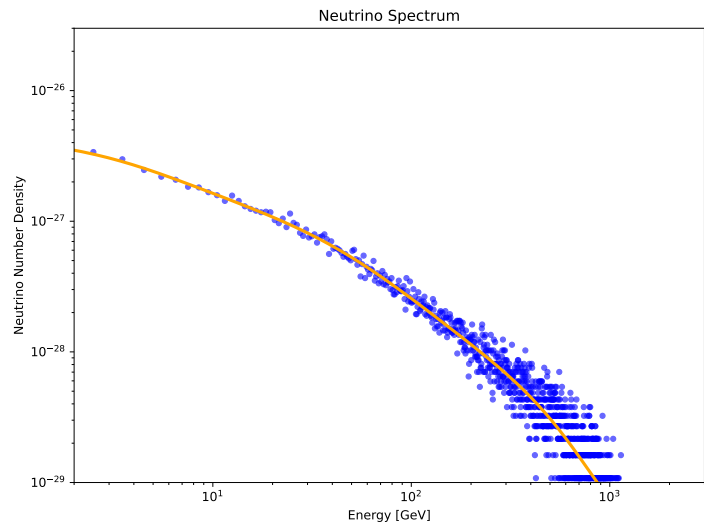


Figure 4. Differential energy spectrum of neutrinos per 2.5 TeV color octet decay.

Figures 3 and 4 display the resulting differential spectra $dN/dVdE$ of photons and neutrinos. Since other stable particles contribute negligibly, high-energy gamma-ray and neutrino observatories offer the best discovery prospects for the color-octet scalar in astrophysical observations.

5.2 Phenomenology of a massive gluon

In our scenario the $SU(3)_c$ symmetry breaks to $U(2)$, leaving four gluons massless while the remaining four acquire a common mass of order

$$M_g \sim g_s \psi_0 \approx 1 \text{ TeV}, \quad (5.8)$$

where g_s is the strong coupling evaluated at the TeV scale, and $\psi_0 \sim 1 \text{ TeV}$ is the vacuum expectation value of the adjoint scalar in the true minimum. The remaining four gluons stay massless inside the broken phase and are associated with the unbroken $U(2)$ subgroup rather than with ordinary $SU(3)_c$ QCD.

Inside the true vacuum bubble, the residual unbroken gauge sector mediates the strong dynamics responsible for the formation of bound states of the massive gluons. More precisely, the non-Abelian $SU(2) \subset U(2)$ part is expected to remain asymptotically free and confining in the infrared, while the Abelian $U(1)$ factor mediates long-range Coulombic interactions. At short distances, where asymptotic freedom holds, the inter-gluon potential may be modeled approximately as Coulombic,

$$V(r) \simeq -\frac{C_{\text{eff}} \alpha_{\text{eff}}}{r}, \quad (5.9)$$

while at larger separations, confinement induces a linear potential, σr , yielding an overall Cornell-type form,

$$V(r) = -\frac{C_{\text{eff}} \alpha_{\text{eff}}}{r} + \sigma r, \quad (5.10)$$

as in the case of heavy quarkonia [85, 86]. Solving the Schrödinger equation in this hybrid potential gives the typical size of the lowest bound states. In the Coulombic region, a Bohr-model estimate analogous to positronium applies because both constituents have the same mass:

$$r_B \sim \frac{1}{M_g \alpha_s(M_g)}. \quad (5.11)$$

For $M_g \simeq 1 \text{ TeV}$ and $\alpha_s(M_g) \simeq 0.08$,¹ one obtains $r_B \approx 2.5 \times 10^{-18} \text{ m}$, which is about an order of magnitude larger than the Compton wavelength of the gluon $\lambda_C = \hbar c/M_g \approx 2 \times 10^{-19} \text{ m}$. At this distance, the Yukawa suppression factor for exchange of the heavy broken gluons is

$$e^{-M_g r_B} = e^{-1/\alpha_s(M_g)} \approx e^{-12.5} \approx 4 \times 10^{-6}, \quad (5.12)$$

demonstrating that direct exchange of the heavy broken gluons between such bound states is exponentially small. Thus, the heavy-gluon dynamics are expected to be dominated by the unbroken gauge interaction, whose potential determines the structure and size of the bound states. This is also consistent with the effective-field-theory expectation that sufficiently heavy broken-sector gauge bosons decouple from long-distance dynamics, in the spirit of Appelquist–Carazzone [87], and with the expectation that the confinement radius is set by the infrared scale of the unbroken non-Abelian sector as argued by Goncharov [88].

¹For order-of-magnitude estimates we use the Standard-Model QCD coupling evaluated at the TeV scale as a proxy for the broken-phase non-Abelian coupling; a dedicated renormalization-group treatment of the residual $U(2)$ theory is left for future work.

This behavior is analogous to the hierarchy observed in heavy-quark systems such as charmonium and bottomonium, where the bound-state size scales as $1/(m_Q\alpha_s)$ and the potential interpolates smoothly between Coulombic and confining regimes. In the present scenario, the corresponding heavy-gluon bound states are considerably more compact, but their sizes remain controlled by the same parametric scaling, ensuring that their formation and decay dynamics mirror those of conventional heavy quarkonia at proportionally higher mass scales.

In contrast, outside the bubble—the false vacuum corresponding to the Standard Model QCD phase—the confinement scale remains $\Lambda_{\text{QCD}}^{\text{SM}} \sim 100$ MeV. There, the typical hadron radius made up of light quarks is $r_{\text{hadron}}^{\text{SM}} \sim 1$ fm, while the TeV-scale gluon has a range $\lambda_C \sim 10^{-18}$ m $\ll r_{\text{hadron}}^{\text{SM}}$. Consequently, the Yukawa factor $e^{-M_g r}$ becomes exponentially small, and the heavy gluon completely decouples from low-energy hadronic physics, as expected. Outside the bubble, ordinary $SU(3)_c$ QCD is recovered, whereas inside the true vacuum the long-distance dynamics are governed by the residual $U(2)$ gauge theory and therefore differ qualitatively from standard QCD.

For our current study, we are mostly interested in the decays of the massive gluons. In the leading order, a massive gluon G^a (with adjoint index a) decays into quark–antiquark pairs through the usual QCD interaction

$$\mathcal{L}_{\text{int}} = g_s \bar{q}_i \gamma^\mu T_{ij}^a q_j G_\mu^a. \quad (5.13)$$

In this framework, the tree-level partial width for $G \rightarrow q\bar{q}$ can be derived from color, spin, and two-body phase space (see Appendix D). Summing over final-state colors and spins and averaging over the three initial polarizations of a massive vector yields

$$\Gamma(G \rightarrow q\bar{q}) = \frac{\alpha_s}{6} M_g \left(1 + \frac{2m_q^2}{M_g^2}\right) \sqrt{1 - \frac{4m_q^2}{M_g^2}}. \quad (5.14)$$

The coefficient $1/6$ arises from the fundamental color factor $T(R) = \frac{1}{2}$, the average over three vector polarizations ($2J+1 = 3$), and the standard $1 \rightarrow 2$ phase-space normalization.

The kinematic factor $\sqrt{1 - 4m_q^2/M_g^2}$ ensures that for $M_g < 2m_q$ the decay is forbidden, rising smoothly from zero at the threshold $M_g = 2m_q$. The prefactor $(1 + 2m_q^2/M_g^2)$ gives a modest enhancement near threshold (notably for top). Expanding near threshold,

$$\Gamma \propto \alpha_s M_g \sqrt{\delta}, \quad \delta = 1 - \frac{4m_q^2}{M_g^2}. \quad (5.15)$$

In the limit where the gluon mass greatly exceeds all quark masses ($M_g \gg m_q$), mass-dependent corrections become negligible and the partial widths simplify to

$$\Gamma(G \rightarrow q\bar{q}) \simeq \frac{\alpha_s}{6} M_g. \quad (5.16)$$

Since every quark flavor above threshold contributes equally, the branching fractions approach a universal value:

$$\text{BR}(G \rightarrow q\bar{q}) \simeq \frac{1}{N_f}, \quad (5.17)$$

where N_f is the number of kinematically open flavors. For $M_g > 2m_t$, one has $N_f = 6$, yielding $\text{BR} \approx 16.7\%$ for each quark species.

5.2.1 Branching ratio and decay width at $M_g \sim 1$ TeV.

The branching ratios and decay widths of the massive gluons to different quarks are listed in Table 2, using $\alpha_s(1 \text{ TeV}) = 0.09$ and $m_t = 173 \text{ GeV}$.

Gluon mass $M_g = 1 \text{ TeV}$		
Total decay width: 89.91 GeV		
Quark	Decay Width (GeV)	BR (%)
up	15.00	16.68
down	15.00	16.68
strange	15.00	16.68
charm	15.00	16.68
bottom	15.00	16.68
top	14.91	16.59

Table 2. Partial widths and branching ratios for a 1 TeV massive gluon at tree level, using Eq. (5.14) with $\alpha_s = 0.09$.

Summing over the six kinematically accessible quarks yields

$$\Gamma_{\text{tot}} \simeq 89.91 \text{ GeV}, \quad \frac{\Gamma}{M_g} \sim 0.09,$$

for a gluon mass of 1 TeV. The branching ratio of the top channel rises from its threshold-suppressed value and approaches the democratic limit of 16.7% as the gluon mass increases and the kinematic suppression becomes negligible.

5.2.2 Hadronization and final-state yields

The six partial widths and branching ratios calculated for a 1 TeV gluon—with a total width of $\simeq 89.9 \text{ GeV}$ and each light-flavor channel at roughly 16.7% (top quark at 16.6%)—were used directly as the hard-process input in `Pythia8` [59, 60]. `Pythia` then handled the fragmentation of every $q\bar{q}$ pair into hadrons (mesons and baryons) and simulated the decays of all unstable resonances.

Inside each jet, neutral pions ($\pi^0 \rightarrow \gamma\gamma$) are produced in great abundance, while charged pions, kaons and heavy-flavor hadrons undergo semileptonic decays that yield high-energy neutrinos. As a result, the photon and neutrino counts per gluon decay exceed those of any other stable particle species (electrons, muons, protons, neutrons, etc.) by more than an order of magnitude. This makes high-energy photons and neutrinos the most distinctive, long-range observational signatures of TeV-scale gluon decay.

Figure 5 displays the differential energy spectra $dN/dVdE$ of photons and neutrinos, respectively, for the 1 TeV gluon. Because contributions from other stable particles are negligible, searches with gamma-ray and neutrino observatories provide the most sensitive means to detect these massive-gluon decay signals. The spectra in Figures 3, 5 and 4, show the photon and neutrino number density respectively at the site of creation. To obtain the spectra that can be observed on Earth, we have to take their propagation into account.

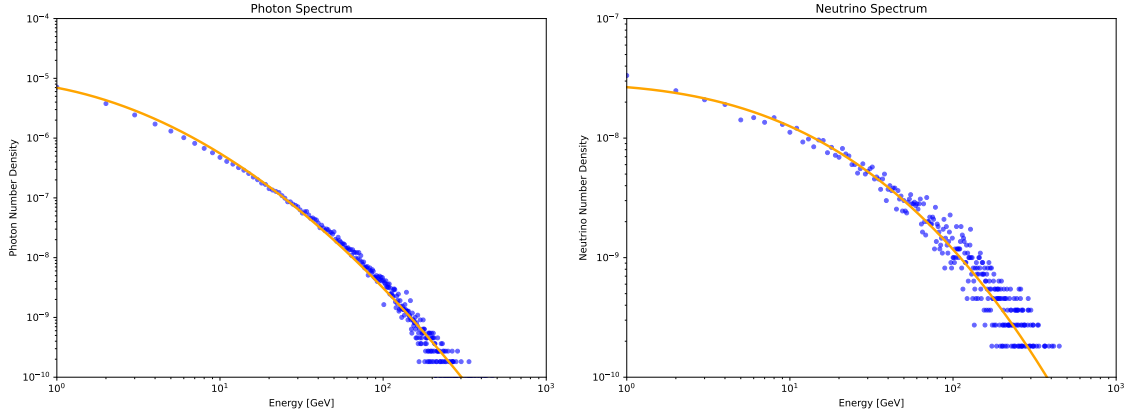


Figure 5. Differential energy spectrum of photons and neutrinos per 1 TeV massive gluon decay.

The corresponding particle flux, i.e. the number of particles per unit area per unit time, is diluted by a factor of $1/[4\pi d^2(1+z)]$, where d is the physical distance between the source and the observer, while z is the redshift of the source. The factor $(1+z)$ appears due to the relativistic time delay because particles hit the sphere with the radius d less frequently (two particles emitted Δt apart will be measured $(1+z)\Delta t$ apart). We also have to correct the particle energies by a factor of $1+z$ because the individual particle’s energies are redshifted by that factor.

6 Relativistic bubble–wall dynamics in a viscous medium and terminal velocity

If the bubble wall moves with the speed of light, then no signal can overtake it to warn us about the impending doom. However, expansion of a vacuum bubble is generically impeded by interactions with its environment, i.e. matter or radiation (where some of it could be produced by the bubble itself). The wall therefore tends to approach a subluminal terminal speed rather than accelerating indefinitely. In this work we use the relativistic thin–wall framework developed in our earlier analysis of Higgs–vacuum decay with friction [5, 89], and we adapt it to the present $SU(3)_c$ –breaking setting (see also [22, 90–101] for related discussions of wall friction and hydrodynamics). For completeness, we collect the working equations needed below and record the $SU(3)_c$ model–specific normalizations.

6.1 Equation of motion and terminal balance

In the thin–wall description the rest energy per unit area equals the surface tension σ . Under a boost with speed v the wall carries energy density $\sigma\gamma(v)$ and momentum density $\sigma\gamma(v)v$, with $\gamma(v) = (1-v^2)^{-1/2}$. Balancing the time derivative of the momentum density against the net outward force density (vacuum pressure jump, curvature pressure, and linear drag) gives the relativistic spherical EOM [5]:

$$\sigma\gamma^3(v)\frac{dv}{dt} = \Delta V - \frac{2\sigma}{R(t)} - \eta\gamma(v)v, \quad (6.1)$$

where $R(t)$ is the instantaneous radius, $\Delta V \equiv V_{\text{false}} - V_{\text{true}}$ is the driving pressure (latent heat), and η is the effective linear friction coefficient encoding wall–medium interactions.

At terminal motion the acceleration vanishes and Eq. (6.1) reduces to

$$0 = \Delta V - \frac{2\sigma}{R} - \eta\gamma(v)v \quad \iff \quad \Delta V_{\text{eff}}(R) \equiv \Delta V - \frac{2\sigma}{R} = \eta\gamma(v)v, \quad (6.2)$$

so in the large- R (planar) limit the terminal relation is simply $\Delta V = \eta\gamma v$.

For the $SU(3)_c$ potential specified in Sec. 2, the quantities that enter Eq. (6.1) are

$$\Delta V = \frac{9}{4}\epsilon_0\psi_0^4, \quad \sigma \simeq \sqrt{\frac{\lambda_1}{8}}\psi_0^3, \quad (6.3)$$

so that

$$A \equiv \frac{\Delta V}{\sigma} = \frac{3}{R_0}, \quad (6.4)$$

with R_0 the thin-wall nucleation radius. Equation (6.4) fixes the initial drive used below.

6.2 Proper-time formulation

Following [5], it is convenient to parametrize the motion by the wall's proper time τ and rapidity $y(\tau)$,

$$v = \tanh y, \quad \gamma = \cosh y, \quad \gamma v = \sinh y, \quad \frac{dt}{d\tau} = \gamma, \quad \frac{dR}{d\tau} = \gamma v = \sinh y. \quad (6.5)$$

The proper acceleration is

$$\alpha(\tau) \equiv \gamma^3 \frac{dv}{dt} = \frac{dy}{d\tau}. \quad (6.6)$$

Dividing Eq. (6.1) by σ and using (6.6) yields

$$\frac{dy}{d\tau} = A - \frac{2}{R(\tau)} - B \sinh y(\tau), \quad A \equiv \frac{\Delta V}{\sigma}, \quad B \equiv \frac{\eta}{\sigma}, \quad (6.7)$$

$$\frac{dt}{d\tau} = \cosh y, \quad \frac{dR}{d\tau} = \sinh y. \quad (6.8)$$

With nucleation data $R(0) = R_0$ and $y(0) = 0$, one has

$$\alpha(0) = A - \frac{2}{R_0} \simeq \frac{1}{R_0}, \quad (6.9)$$

where the final step uses $A = 3/R_0$ from Eq. (6.4).

For proper times $\tau \ll R_0$ the motion is only mildly relativistic. With $y(\tau) = \alpha(0)\tau + \mathcal{O}(\tau^2)$ and $\sinh y \simeq y$ one finds

$$\sinh y(\tau) \simeq \alpha(0)\tau, \quad R(\tau) \simeq R_0 + \int_0^\tau \sinh y d\tau' \simeq R_0 + \frac{\alpha(0)}{2}\tau^2. \quad (6.10)$$

Inserting (6.10) into $\alpha(\tau) = A - \frac{2}{R(\tau)} - B \sinh y(\tau)$ [Eq (6.7)] gives the leading drag and curvature pieces $-B\alpha(0)\tau$ and $+\alpha(0)\tau^2/R_0^2$, so the proper acceleration expands as

$$\alpha(\tau) \simeq \underbrace{\left(A - \frac{2}{R_0}\right)}_{\alpha(0)} - B\alpha(0)\tau + \frac{\alpha(0)}{R_0^2}\tau^2 + \mathcal{O}(\tau^3). \quad (6.11)$$

Using $A \simeq 3/R_0$ implies $\alpha(0) \simeq 1/R_0$, yielding

$$\alpha(\tau) \simeq \frac{1}{R_0} - \frac{B}{R_0}\tau + \frac{\tau^2}{R_0^3} + \mathcal{O}(\tau^3), \quad (6.12)$$

valid for $\tau \ll R_0$ (so $y \ll 1$) and weak friction in the sense $BR_0 \ll 1$. The linear term $-(B/R_0)\tau$ arises from viscous drag, whereas the quadratic term $+\tau^2/R_0^3$ reflects the relaxation of the contribution to curvature as R grows.

6.3 Evolution of the proper acceleration and approach to terminal motion

Differentiating Eq. (6.7) and using $\frac{dR}{d\tau} = \sinh y$ and $\frac{dy}{d\tau} = \alpha$ yields the exact evolution equation

$$\frac{d\alpha}{d\tau} = \frac{2}{R^2} \frac{dR}{d\tau} - B \cosh y \frac{dy}{d\tau} = \frac{2 \sinh y}{R^2} - B \cosh y \alpha. \quad (6.13)$$

In the planar, small-rapidity limit ($R \rightarrow \infty$, $\cosh y \simeq 1$) one has $d\alpha/d\tau \simeq -B\alpha$, hence

$$\alpha(\tau) \simeq \alpha(0) e^{-B\tau}, \quad \tau_{\text{term}} \equiv \frac{1}{B} = \frac{\sigma}{\eta}, \quad (6.14)$$

which defines the characteristic proper-time to approach terminal motion. As $R \rightarrow \infty$ the curvature term disappears and (6.8) reduces to

$$\alpha(\tau) \rightarrow A - B \sinh y(\tau). \quad (6.15)$$

At terminal balance ($\alpha \rightarrow 0$) the rapidity satisfies

$$\sinh y_{\text{term}} = \frac{A}{B} \iff \gamma_{\text{term}} v_{\text{term}} = \frac{\Delta V}{\eta}, \quad (6.16)$$

the planar version of Eq. (6.2). These relations, taken together with the $SU(3)_c$ identification $A = 3/R_0$, are the inputs we use to benchmark wall velocities and to delimit the acceleration-driven particle-production epoch in the remainder of this work.

7 Particle production with frictional effects due to vacuum mismatch

We now turn to the $SU(3)_c$ model, where the expansion of the bubble wall in the broken phase produces massive gluons and associated colored scalars. Our goal is to estimate the number of quanta produced in the regime prior to saturation at terminal velocity. For clarity we work here in TeV units. The relevant parameters determined by the potential in Sec. 2 are

$$\begin{aligned} \psi_0 &= 0.983271 \text{ TeV}, & \Delta V &= 1.598416 \times 10^{-1} \text{ TeV}^4, & \sigma &= 3.361052 \times 10^{-1} \text{ TeV}^3, \\ R_0 &= 6.308219 \text{ TeV}^{-1}, & A &= 0.475570 \text{ TeV}, & \mu_s &= 2.480876 \text{ TeV}. \end{aligned} \quad (7.1)$$

The dimensionless drive and friction ratios are defined analogously,

$$A \equiv \frac{\Delta V}{\sigma}, \quad B \equiv \frac{\eta}{\sigma}, \quad (7.2)$$

and the bubble wall kinematics are parametrized by its proper time τ and rapidity $y(\tau)$,

$$v = \tanh y, \quad \gamma = \cosh y, \quad \gamma v = \sinh y, \quad \frac{dt}{d\tau} = \gamma, \quad \frac{dR}{d\tau} = \sinh y. \quad (7.3)$$

The proper acceleration that governs particle production is

$$\alpha(\tau) \equiv \frac{dy}{d\tau} = A - \frac{2}{R(\tau)} - B \sinh y(\tau), \quad (7.4)$$

with initial conditions

$$R(0) = R_0, \quad y(0) = 0, \quad t(0) = 0, \quad N_{\text{tot}}(0) = 0. \quad (7.5)$$

$\alpha(0) = A - 2/R_0 \simeq 1/R_0$ under the thin-wall relation $A \simeq 3/R_0$.

The instantaneous zero momentum mode occupancy at a proper time τ is taken from the vacuum-mismatch procedure derived in the previous sections by replacing the constant proper acceleration with the time dependent one from this section

$$N_{k=0}(\tau) = \left[\frac{(\omega_+ + \omega_-)^2}{(\omega_+ - \omega_-)^2} \exp\left(\frac{4\omega_+}{\alpha(\tau)}\right) - 1 \right]^{-1}, \quad (7.6)$$

with $\omega_+ = \mu_s$ and $\omega_- = M_s$, while for the massive-gluon channel we use $\omega_+ = \mu_g$ and $\omega_- = 0$ in the true and false vacuum respectively. The total number evolves as

$$\frac{dN_{\text{tot}}}{d\tau} = N_{k=0}(\tau) 4\pi R(\tau)^2 \sinh y(\tau), \quad (7.7)$$

and is accumulated numerically until the wall reaches its terminal velocity, $\tau = \tau_{\text{term}} = \sigma/\eta$. $N_{k=0}^{(\text{int})}$ denotes the accumulated yield obtained by integrating the production rate from nucleation up to time τ . Thus at $\tau = 0$, no time or volume has yet been accumulated, so $N_{k=0}^{(\text{int})}(0) = 0$. By contrast, $N_{k=0}(0)$ is an instantaneous occupation density; it contributes to the total only after integrating over a finite interval and swept volume. The details of the numerical calculation have been described in Appendix I and here we list the results in the following Table 3

Scenario	η [TeV ⁴]	τ_{term} [TeV ⁻¹]	R_{fin} [TeV ⁻¹]	Scalars- $N_{\text{tot}}^{(\text{int})}$	Massive Gluons- $N_{\text{tot}}^{(\text{int})}$
$\delta = 10^{-12}$	2.260×10^{-7}	1.487×10^6	1.051×10^{12}	6.101×10^6	4.881×10^7
$\delta = 10^{-11}$	7.148×10^{-7}	4.702×10^5	1.051×10^{11}	1.928×10^5	1.542×10^6
$\delta = 10^{-10}$	2.261×10^{-6}	1.487×10^5	1.051×10^{10}	6.087×10^3	4.869×10^4

Table 3. For each ultra-relativistic deficit $\delta = 1 - v_{\text{term}}$ we evolve the $SU(3)_c$ bubble wall using (7.4) until $\tau_{\text{term}} = \sigma/\eta$ is reached. The total yields $N_{\text{tot}}^{(\text{int})}$ are shown separately for a single scalar degree of freedom and for the four massive-gluons (transverse polarizations only). Only the $k = 0$ mode quanta are included; higher- k modes would increase the total particle production.

In this subsection we deliberately adopt a simplified description in which the drag coefficient η is taken to be constant, so that the dimensionless friction ratio $B = \eta/\sigma$ in Eq. (7.4) does not depend on the state of the shocked plasma. The purpose of this

discussion is to isolate the pure “vacuum–mismatch” contribution to particle production: the accelerating wall imposes a time–dependent boundary condition on the relevant quantum fields, and the non–adiabatic change in the mode frequencies ω_{\pm} produces quanta even in the absence of an explicitly thermalised medium. The resulting zero–mode occupancy $N_{k=0}(\tau)$ in Eqs. (7.6)–(I.5) should therefore be viewed as a minimal, non–thermal lower bound on the particle yield associated with the acceleration history of the wall.

Using the benchmark values from Table-3, the typical vacuum energy difference is $\Delta V \simeq 0.16 \text{ TeV}^4$. The total energy released as the wall expands to its final radius is then

$$E_{\text{vac}} = \Delta V \int_{R_0}^{R_{\text{fin}}} 4\pi R^2 dR = \frac{4\pi}{3} \Delta V (R_{\text{fin}}^3 - R_0^3). \quad (7.8)$$

For $R_{\text{fin}} \gg R_0$, this simplifies to

$$E_{\text{vac}} \simeq \frac{4\pi}{3} \Delta V R_{\text{fin}}^3, \quad (7.9)$$

numerically

$$E_{\text{vac}} \approx \begin{cases} 6.7 \times 10^{35} \text{ TeV}, & \delta = 10^{-12}, \\ 6.7 \times 10^{32} \text{ TeV}, & \delta = 10^{-11}, \\ 6.7 \times 10^{29} \text{ TeV}, & \delta = 10^{-10}. \end{cases}$$

Even if only a minute fraction of this energy converts into rest mass, it readily accounts for the creation of multi–TeV particles. The accelerating wall imposes a time–dependent boundary condition on the surrounding quantum fields. As this boundary moves, the vacuum configuration changes, and the inertial observer perceives particle creation. Only fields that couple to the boundary respond to this varying condition; uncoupled fields remain unaffected. This process resembles a dynamical Casimir effect, where the moving boundary extracts energy from the vacuum and converts it into real particles. This viewpoint is not in conflict with the earlier Unruh–like interpretation: the Unruh description highlights the role of the wall’s proper acceleration, whereas the dynamical–Casimir description highlights the non–adiabatic change of the field modes induced by the moving wall. In the present setup these should be understood as complementary interpretations of the same underlying particle–production mechanism. Thus, the large vacuum pressure driving the bubble expansion provides the true energy reservoir for producing massive quanta in the true–vacuum phase.

As the radius increases, drag compensates the vacuum drive and the wall approaches terminal speed on the timescale τ_{term} . The total yield reflects the competition between the exponential sensitivity of $N_{k=0}(\alpha)$ to the declining acceleration and the rapidly growing area factor $4\pi R^2$, which becomes significant by $\tau \sim \tau_{\text{term}}$ in the most ultra–relativistic cases.

8 Thermal particle production from frictional dissipation in the $SU(3)_c$ transition

As the $SU(3)_c$ –breaking bubble wall propagates through an ambient medium, microscopic scatterings between the wall and the surrounding plasma exert a frictional pressure

$$P_{\text{fric}} = \eta \gamma v, \quad (8.1)$$

which acts against the vacuum–mismatch force responsible for accelerating the wall. In the absence of friction the wall would acquire a large kinetic energy; with friction, part of this energy is continuously drained and deposited into a thin layer of shocked plasma immediately behind the wall. Because the wall is ultra–relativistic, this layer thermalises on timescales that are microscopic compared to the macroscopic wall evolution. Our goal in this section is to quantify the corresponding thermal energy and the resulting number of thermal quanta produced in the broken $SU(3)_c$ phase.

The treatment presented here follows the same energy–deficit logic as in our previous false Higgs vacuum decay analysis in Section 7 of Ref. [5], but is now implemented in a fully microscopic $SU(3)_c$ setup with TeV–scale parameters and with an explicit separation between a scalar degree of freedom and the massive gluon sector. For a more detailed conceptual discussion of the energy–deficit framework, we refer the reader to Ref. [5]. We do not assume any specific underlying microphysics for the friction; instead, all dissipative effects are encoded in the difference between a frictionless bubble trajectory and the corresponding friction–limited trajectory, which is then promoted into a local heating rate. In principle, once the wall enters a quasi-steady-state regime, direct scattering and momentum transfer of ambient particles across the moving wall can provide an additional source of particle production, as emphasized in microscopic studies of bubble-wall friction and transition-radiation effects [90, 91, 95, 102]; however, in the present setup we expect this contribution to be subdominant compared with the thermal particle production generated by the much larger frictional energy dissipated into the shocked medium, and we therefore do not discuss it here.

Local energy conservation and the energy deficit

The energy stored in the wall per unit area is

$$E_{\text{wall}}(t) = \sigma \gamma(t), \quad \gamma(t) = \frac{1}{\sqrt{1 - v^2(t)}}, \quad (8.2)$$

where σ is the surface tension of the $SU(3)_c$ domain wall and $v(t)$ is the wall velocity in the rest frame of the ambient medium. Curvature modifies the acceleration via the usual Laplace pressure term $2\sigma/R$, but does not change the form of the boosted surface energy density.

To track dissipation we compare two trajectories:

- (i) a *frictionless* wall with velocity $v_0(t)$ and Lorentz factor $\gamma_0(t)$, and
- (ii) the *physical* wall, whose acceleration is reduced by friction and moves with velocity $v(t)$ and Lorentz factor $\gamma(t)$.

The frictionless wall obeys

$$\sigma \gamma_0^3 \frac{dv_0}{dt} = \Delta V - \frac{2\sigma}{R}, \quad (8.3)$$

where ΔV is the vacuum–energy difference across the wall and $R(t)$ is the bubble radius. In turn, the friction–limited wall satisfies

$$\sigma \gamma^3 \frac{dv}{dt} = \Delta V - \frac{2\sigma}{R} - \eta \gamma v, \quad (8.4)$$

where the last term represents the drag exerted by the medium.

The key identity

$$\frac{d\gamma}{dt} = \gamma^3 v \frac{dv}{dt} \quad (8.5)$$

relates changes in the Lorentz factor directly to changes in velocity. Applying it to the frictionless trajectory gives

$$\begin{aligned} \frac{d\gamma_0}{dt} &= \gamma_0^3 v_0 \frac{dv_0}{dt} = \gamma_0^3 v_0 \left(\frac{\Delta V - 2\sigma/R}{\sigma \gamma_0^3} \right) \\ \Rightarrow \frac{d\gamma_0}{dt} &= \frac{v_0}{\sigma} \left(\Delta V - \frac{2\sigma}{R} \right), \end{aligned} \quad (8.6)$$

and an analogous expression holds for the frictional trajectory,

$$\frac{d\gamma}{dt} = \frac{v}{\sigma} \left(\Delta V - \frac{2\sigma}{R} - \eta \gamma v \right). \quad (8.7)$$

The maximal wall energy per unit area that would be reached in the absence of friction is

$$E_{\max}(t) = \sigma \gamma_0(t), \quad E_{\text{wall}}(t) = \sigma \gamma(t), \quad (8.8)$$

so that the difference

$$\Delta E(t) = \sigma [\gamma_0(t) - \gamma(t)] \quad (8.9)$$

measures the kinetic energy that the wall *would* have gained but did not. This energy deficit is the true measure of dissipation. Differentiating and using Eqs. (8.6) and (8.7) yields the master relation

$$\frac{d}{dt} \Delta E(t) = (v_0 - v) \left(\Delta V - \frac{2\sigma}{R} \right) + \eta \gamma v^2. \quad (8.10)$$

Both terms vanish when $\eta \rightarrow 0$, as required.

Thermalisation in a finite comoving layer

The energy lost by the wall is deposited into a thin shocked region of the plasma behind the wall. We model this region as a comoving layer of proper thickness ℓ and area $A(t) = 4\pi R^2(t)$. The total thermal energy is then

$$E_{\text{th}}(t) = \rho_{\text{th}}(t) A(t) \ell, \quad (8.11)$$

and local energy conservation requires that the thermal energy per unit area equals the accumulated deficit,

$$\rho_{\text{th}}(t) \ell = \Delta E(t). \quad (8.12)$$

Differentiation gives

$$\frac{d\rho_{\text{th}}}{dt} = \frac{1}{\ell} \frac{d}{dt} \Delta E(t), \quad (8.13)$$

so that, inserting Eq. (8.10),

$$\frac{d\rho_{\text{th}}}{dt} = \frac{1}{\ell} \left[(v_0 - v) \left(\Delta V - \frac{2\sigma}{R} \right) + \eta \gamma v^2 \right]. \quad (8.14)$$

Switching to proper time $d\tau = dt/\gamma$ we obtain

$$\frac{d\rho_{\text{th}}}{d\tau} = \frac{\gamma}{\ell} \left[(v_0 - v) \left(\Delta V - \frac{2\sigma}{R} \right) + \eta \gamma v^2 \right]. \quad (8.15)$$

In the $SU(3)_c$ setup the microscopic scale that controls both the wall thickness and the range of the interactions in the broken phase is set by the TeV-scale masses of the heavy modes. For the scalar we can write

$$\mu_s \equiv M_{G_H} = 2.5 \text{ TeV}, \quad (8.16)$$

while the massive gluons have a characteristic mass

$$\mu_g \equiv M_g \simeq 1 \text{ TeV}, \quad (8.17)$$

set by the $SU(3)_c \rightarrow U(2)$ breaking scale. It is natural to assume that the thermalised layer in each channel cannot be parametrically thinner than the corresponding wall thickness, so that

$$\ell_s \sim \frac{1}{\mu_s}, \quad \ell_g \sim \frac{1}{\mu_g}, \quad (8.18)$$

for the scalar and gluon components respectively. In practice we implement this by introducing separate energy densities ρ_s and ρ_g for the scalar and gluon sectors, each obeying

$$\frac{d\rho_i}{d\tau} = \mu_i \left[\gamma(v_0 - v) \left(\Delta V - \frac{2\sigma}{R} \right) + \eta \gamma^2 v^2 \right], \quad i = s, g, \quad (8.19)$$

where μ_s and μ_g appear as the inverse comoving thicknesses ℓ_i^{-1} . We model the sector dependence by assuming that the effective thermalization thickness is set by the inverse mass scale of the corresponding heavy mode, $\ell_i \sim \mu_i^{-1}$.

8.1 Thermal particle production in the scalar and gluon channels

Once the thermal energy densities $\rho_s(\tau)$ and $\rho_g(\tau)$ are known, the corresponding temperatures follow from equilibrium thermodynamics,

$$T_i(\tau) = \left(\frac{30}{\pi^2 g_*} \rho_i(\tau) \right)^{1/4}, \quad i = s, g, \quad (8.20)$$

where we take $g_* = 106.75$ to represent the effective number of relativistic degrees of freedom in the thermal bath. For each sector the equilibrium number density of bosons is

$$n_i(\tau) = \frac{\zeta(3)}{\pi^2} g_i T_i(\tau)^3, \quad g_s = 1, \quad g_g = 8, \quad (8.21)$$

where g_s and g_g are the degeneracies of the Higgs-like scalar and of the massive gluons respectively (four massive gluons with two polarisations each).² For the benchmark shown below, the bubble wall moves in an ultra-relativistic regime, and the shock temperatures we obtain are well above the corresponding heavy masses, $T_s \gg \mu_s$ and $T_g \gg \mu_g$. In other

²We are keeping only the transverse polarizations in the thermal sector as a conservative lower bound.

words, not only the wall itself but also the thermally produced scalar and gluon quanta are highly relativistic. This makes the use of the standard relativistic equilibrium estimates, $n_i \propto T_i^3$ well justified for the parameter range considered here.

As the wall advances it sweeps out a comoving volume

$$dV = 4\pi R^2(\tau) \sinh y(\tau) d\tau, \quad (8.22)$$

so that the instantaneous thermal production rates are

$$\frac{dN_s}{d\tau} = 4\pi R^2(\tau) \sinh y(\tau) n_s(\tau), \quad (8.23)$$

$$\frac{dN_g}{d\tau} = 4\pi R^2(\tau) \sinh y(\tau) n_g(\tau), \quad (8.24)$$

and the corresponding total multiplicities at the end of the evolution are

$$N_s = N_s(\tau_{\text{final}}), \quad N_g = N_g(\tau_{\text{final}}). \quad (8.25)$$

By construction, the scalar and gluon sectors share the same heating history through the common bracket in Eq. (8.19), but their final multiplicities differ because of their distinct microscopic scales μ_i and degeneracies g_i .

Numerical procedure and choice of parameters

We follow a numerical procedure closely analogous to the one used for the electroweak transition in Ref [5], but now specialised to $SU(3)_c$ breaking scenario. The dynamical system solved numerically is

$$\left\{ \frac{dR}{d\tau}, \frac{dy}{d\tau}, \frac{dR_{fr}}{d\tau}, \frac{dy_{fr}}{d\tau}, \frac{d\rho_s}{d\tau}, \frac{d\rho_g}{d\tau}, \frac{dN_s}{d\tau}, \frac{dN_g}{d\tau} \right\}, \quad (8.26)$$

where the frictionless variables (R_{fr}, y_{fr}) are evolved in parallel with the physical variables (R, y) using Eqs. (8.3) and (8.4). The heating equations for ρ_s and ρ_g follow from Eq. (8.19), and the number densities and multiplicities are updated using Eqs. (8.20)–(8.24).³

Astrophysical microphysics is parametrised via the terminal-velocity deficit

$$\delta \equiv 1 - v_{\text{term}}, \quad (8.27)$$

which fixes how close the wall comes to the speed of light before friction balances the vacuum pressure. For a given δ one has

$$v_{\text{term}} = 1 - \delta, \quad \gamma_{\text{term}} = \frac{1}{\sqrt{1 - v_{\text{term}}^2}}. \quad (8.28)$$

In the usual constant-friction picture the force-balance condition

$$\Delta V = \eta(0) \gamma_{\text{term}} v_{\text{term}} \quad (8.29)$$

³The sector-resolved quantities ρ_s and ρ_g are introduced here as an effective phenomenological split of the dissipated energy, intended to track separately the scalar and massive-gluon contributions to the thermal yield.

would determine a unique drag coefficient

$$\eta(0) = \frac{\Delta V}{\gamma_{\text{term}} v_{\text{term}}}. \quad (8.30)$$

Smaller δ corresponds to more ultra-relativistic walls and hence smaller η_{target} .

In reality the friction is not constant: as the wall dumps energy into the plasma, the shocked layer heats up and pushes back more strongly. To capture this we promote the drag coefficient to a temperature-dependent quantity

$$\eta(\tau) = g_{\text{eff}}^2 T_{\text{eff}}^4(\tau), \quad (8.31)$$

where g_{eff} is an effective coupling which encodes how efficiently the hot plasma transfers momentum to the wall and $T_{\text{eff}}(\tau)$ is an effective temperature combining an ambient seed temperature with the dynamically generated shock temperature,

$$T_{\text{eff}}^4(\tau) = T_{\text{amb}}^4 + T_{\text{shock}}^4(\tau), \quad T_{\text{shock}}^4(\tau) = \frac{30}{\pi^2 g_*} [\rho_s(\tau) + \rho_g(\tau)]. \quad (8.32)$$

This form can be motivated by simple kinetic theory: the drag is proportional to the momentum flux carried by thermal particles, which scales as $np \sim T^3 \times T \sim T^4$, and to the probability $\sim g_{\text{eff}}^2$ that these particles scatter and transfer their momentum to the wall. The combination $\eta(\tau)\gamma(\tau)v(\tau)$ in the wall equation of motion then naturally scales as $g_{\text{eff}}^2 T_{\text{eff}}^4$, corresponding to an energy density loss rate $\propto g_{\text{eff}}^2 T_{\text{eff}}^4$. Parametrically, this choice also matches the behaviour found in detailed electroweak calculations, where the thermal pressure (and hence the effective friction) exerted on an ultrarelativistic bubble wall scales as $P_{\text{th}} \sim \gamma^2 T^4$ up to gauge-coupling factors, see e.g. the all-orders analysis of Ref. [5, 102, 103].

To connect the dynamic ansatz (8.31) to the terminal condition (8.30) we fix, for each δ , the ambient temperature T_{amb} by demanding that at $\tau = 0$ (when $\rho_s = \rho_g = 0$ and $T_{\text{shock}} = 0$) the instantaneous drag reproduces the constant-friction value,

$$\eta(\tau = 0) = g_{\text{eff}}^2 T_{\text{eff}}^4(0) = g_{\text{eff}}^2 T_{\text{amb}}^4. \quad (8.33)$$

This yields

$$T_{\text{amb}} = \left[\frac{\eta(0)}{g_{\text{eff}}^2} \right]^{1/4}. \quad (8.34)$$

In the numerical examples below we adopt

$$g_{\text{eff}} = 10^{-3}, \quad (8.35)$$

so that the subsequent evolution self-consistently increases the friction as the shocked layer heats up, preventing any runaway to Planckian temperatures while keeping the drag anchored to the chosen terminal-velocity deficit.

The wall acceleration timescale is characterised by a reference value

$$\tau_{\text{term}} = \frac{\sigma}{\eta(0)}, \quad (8.36)$$

which is the natural proper-time scale that controls the approach to terminal velocity in the auxiliary constant-friction system with drag coefficient $\eta(0)$. In that simplified model, the solution of the linearised equation of motion from Eqn (8.4) in the late time scenario for a large bubble (neglecting the curvature term) shows an approximately exponential approach to the terminal value, with $\gamma v \rightarrow \gamma_{\text{term}} v_{\text{term}} (1 - e^{-\tau/\tau_{\text{term}}})$, so that a fraction $1 - e^{-\tau/\tau_{\text{term}}}$ of the asymptotic impulse is accumulated by time τ .

In our actual simulations the drag coefficient is not constant but evolves according to $\eta(\tau) = g_{\text{eff}}^2 T_{\text{eff}}^4(\tau)$, with $\eta(0)$ fixed by the terminal condition. The time scale τ_{term} should therefore be interpreted as a convenient normalisation inherited from the constant- η limit rather than as an exact fit to the full non-linear dynamics. We choose the total integration time as

$$\tau_{\text{final}} = k \tau_{\text{term}}, \quad (8.37)$$

with

$$k = 5, \quad \tau_{\text{final}} = 5 \tau_{\text{term}}. \quad (8.38)$$

In the constant-friction toy model this would capture more than 99% of the asymptotic energy deficit, since $1 - e^{-5} \simeq 0.993$, while in the full dynamic- η evolution the increasing friction causes the wall to reach its quasi-terminal regime even faster. We have verified explicitly that increasing k from 5 to 6 changes the final thermal multiplicities by only a few percent, whereas choosing $k = 3$ underestimates them at the tens-of-percent level (see Appendix G for details). The choice $k = 5 \tau_{\text{term}}$ is therefore a conservative and numerically stable benchmark for quoting thermal yields.

Finally, we do not extend the integration arbitrarily far beyond τ_{final} , even though in principle an expanding bubble could continue to radiate and produce particles as long as it cruises near its terminal speed. Our estimate is explicitly local and comoving: the shell is moving relativistically, the radiation it emits is boosted and continues to stream out until it leaves the local horizon, and this outgoing flux induces a radiation-reaction (self-force) on the wall. At the same time, ambient particles in the surrounding medium scatter off the shell, absorb energy, and are scattered away. These two dissipative channels provide additional sources of friction which are effectively encoded in the friction terms we discussed here.

In practice, we find that evolving up to $\tau_{\text{final}} = 5 \tau_{\text{term}}$ already captures the dominant part of the thermal particle production: the multiplicities N_s and N_g change only at the few-percent level if we increase the evolution time further, while shorter runs noticeably underestimate the yields. Extending the integration much beyond this point would not reliably produce more particles within our current setup, because additional physical effects — strong gravity, fully hydrodynamic backreaction of the shocked plasma, and detailed microphysics of radiation reaction and scattering — would start to play an important role. Our choice of a finite τ_{final} should therefore be viewed as a conservative upper bound on the thermal multiplicity within the regime where our approximations remain under quantitative control.

Scenario (δ)	$\eta(0)$ [TeV ⁴]	τ_{final} [TeV ⁻¹]	Scalars N_s	Massive gluons N_g
10^{-12}	2.26×10^{-7}	7.43×10^6	8.61×10^{23}	3.48×10^{24}
10^{-11}	7.15×10^{-7}	2.35×10^6	3.99×10^{22}	1.62×10^{23}
10^{-10}	2.26×10^{-6}	7.43×10^5	1.60×10^{21}	6.49×10^{21}

Table 4. Thermal particle yields in the color octet scalar channel (N_s) and in the massive gluon channel (N_g) obtained from the energy-deficit formulation of the $SU(3)_c$ transition with a temperature-dependent drag coefficient $\eta(\tau) = g_{\text{eff}}^2 T_{\text{eff}}^4(\tau)$ and $g_{\text{eff}} = 10^{-3}$. For each δ , the reference value $\eta(0)$ is fixed by the terminal condition $\Delta V = \eta(0)\gamma_{\text{term}}v_{\text{term}}$, and the evolution is integrated up to $\tau_{\text{final}} = 5\tau_{\text{term}}$.

Numerical results for the $SU(3)_c$ benchmark

For the $SU(3)_c \rightarrow U(2)$ benchmark shown in Fig. 6 we adopt

$$\Delta V = 1.60 \times 10^{-1} \text{ TeV}^4, \quad \sigma = 3.36 \times 10^{-1} \text{ TeV}^3, \quad R_0 = 6.31 \text{ TeV}^{-1}, \quad (8.39)$$

together with $g_* = 106.75$ and $\zeta(3) = 1.202056$. The Higgs-like scalar and massive gluon masses are taken as

$$\mu_s = 2.48 \text{ TeV}, \quad \mu_g = 1.0 \text{ TeV}. \quad (8.40)$$

We consider three ultra-relativistic terminal-velocity deficits,

$$\delta = 10^{-12}, \quad 10^{-11}, \quad 10^{-10},$$

compute $\eta_{\text{target}}(\delta)$ from Eq. (8.30), fix $T_{\text{amb}}(\delta)$ as above, and evolve the system with the dynamic drag coefficient (8.31) up to $\tau_{\text{final}} = 5\tau_{\text{term}}$. The resulting thermal multiplicities and timescales are summarised in Table 4.

The gluon multiplicity is larger than the scalar multiplicity by roughly a factor of four, reflecting the larger degeneracy $g_g = 8$ and the different microscopic scale μ_g , but both sectors exhibit the same qualitative scaling with δ . The total number of heavy quanta produced thermally is enormous, with

$$N_s + N_g \sim 10^{22}\text{--}10^{25} \quad (8.41)$$

over the benchmark range of terminal-velocity deficits. These heavy scalars and gluons are unstable; they promptly decay into lighter Standard Model states, ultimately producing large numbers of photons, neutrinos and charged leptons, together with a potentially observable burst of high-frequency gravitational waves associated with the violent acceleration and shock heating of the wall.

8.2 Thermal spectra for the scalar and gluon sectors

Once the total thermal energy and particle numbers in each sector are known, the momentum distributions of the produced quanta are fixed by equilibrium thermodynamics. For a bosonic species of mass m_i in a thermal bath at temperature T_i the massive Bose-Einstein spectrum is

$$f_i(k) \equiv \frac{k^2}{\exp\left(\sqrt{k^2 + m_i^2}/T_i\right) - 1}, \quad i = s, g, \quad (8.42)$$

where $m_s = \mu_s$ and $m_g = \mu_g$ in the present setup.

The *physically normalised* spectra for the scalar and gluon channels are then defined by

$$\frac{dN_i}{dk} = N_i \frac{f_i(k)}{\int_0^\infty f_i(k) dk}, \quad i = s, g, \quad (8.43)$$

which ensures

$$\int_0^\infty \frac{dN_i}{dk} dk = N_i. \quad (8.44)$$

In each case the peak shock temperature shown in the plots is obtained from the final thermal energy density via

$$T_{\text{peak}} = \left(\frac{30}{\pi^2 g_*} \rho_{\text{th}}(\tau_{\text{final}}) \right)^{1/4}, \quad (8.45)$$

with ρ_{th} the scalar or gluon energy density extracted from the evolution $SU(3)_c$.

Peak structure and scaling. For bosonic thermal distributions with $m \ll T$, the maximum of the momentum distribution occurs very close to

$$k_{\text{peak}} \simeq 2.8 T, \quad (8.46)$$

a standard result that remains accurate for the TeV-scale scalar and massive-gluon masses used in our $SU(3)_c$ benchmark. Because smaller δ leads to much larger thermal energy densities in both the scalar and gluon channels, and thus to larger shock temperatures T , the peaks of the corresponding spectra shift systematically to higher momenta as δ decreases. This scaling, together with the large hierarchy in total particle numbers between the three δ -benchmarks, explains the structure and vertical separation of the curves in the final $SU(3)_c$ spectra.

Resulting thermal spectrum. Figure 6 displays the physically correct, fully normalised spectra dN/dk for the three choices of δ considered in this $SU(3)_c$ setup, shown separately for the scalar and gluon sectors. Each curve encodes: (i) the massive Bose–Einstein shape determined by the corresponding shock temperature, (ii) the shift of the peak at $k_{\text{peak}} \simeq 2.8T$, and (iii) the correct total particle yield fixed by the thermal multiplicities N_{scalar} or N_{gluon} obtained from the microscopic evolution as shown in table 4. The steep decline at $k \gg T$ reflects Boltzmann suppression in the massive tail of the distribution. Although the plots explicitly show the spectra for the $SU(3)_c$ scalar and massive gluons, the same thermal bath also populates all other degrees of freedom with comparable characteristic momenta $k \sim T$, inherited from the same shocked layer.

The resulting thermal channel dominates over vacuum mismatch particle production by many orders of magnitude. This behaviour is expected: once the wall becomes ultra-relativistic, even modest friction injects a substantial fraction of the released vacuum energy into the surrounding medium, and thermalisation converts this into an enormous number of relativistic quanta. While our treatment does not yet include the full fluid back-reaction or plasma self-interaction effects, it serves as a reliable leading-order upper estimate for the

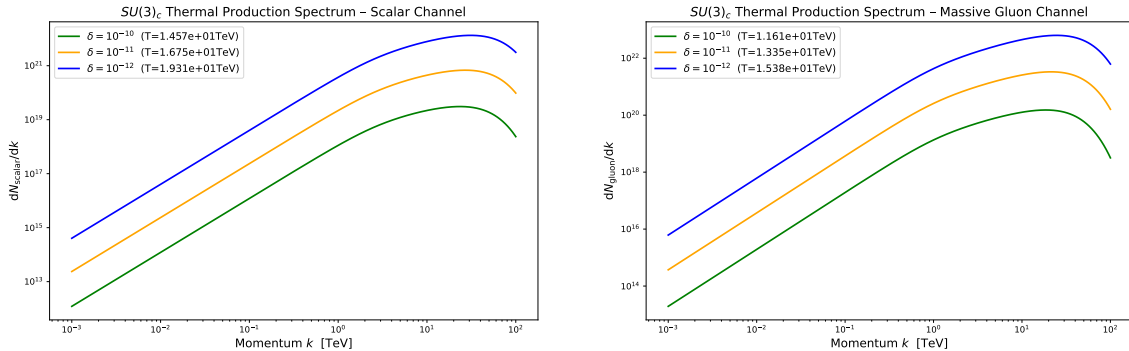


Figure 6. Physically normalised thermal spectra dN_i/dk (differential number density) in the broken $SU(3)_c$ phase for the scalar octet (left, $i = s$) and the massive gluons (right, $i = g$). Each panel shows the spectra for three terminal-velocity deficits $\delta = 10^{-12}$, 10^{-11} , 10^{-10} , with higher curves corresponding to smaller δ . The peak of each distribution lies at $k_{\text{peak}} \sim \mathcal{O}(T_i)$, and the vertical normalisation reflects the physical particle yields N_s and N_g obtained from the energy-deficit evolution and listed in Table 4.

thermal yield, correctly reflecting the primary friction-induced heating and illustrating in a transparent way how an ultra-relativistic wall can inject large amounts of energy into its environment.

The produced excitations are now thermally populated quanta in the shocked layer behind the $SU(3)_c$ bubble wall: a colored octet scalar associated with $SU(3)_c$ breaking and the corresponding massive gluon modes. These degrees of freedom are rapidly thermalised and then promptly decay into QCD final states and subsequent cascades, which in turn generate energetic photons and neutrinos. In the following plots we display the resulting photon and neutrino spectra (differential counts per event versus energy in GeV), which encode both the initial thermal production at the wall and the amplification due to the ultra-relativistic surface expansion.

Once frictional effects are included, the total number of produced quanta is determined by integrating the production rate over the expanding bubble volume. This integration yields a total multiplicity N_{tot} , which effectively rescales the overall normalization of the spectrum without altering its shape. The resulting plots therefore display the fitted spectra, normalized to the integrated yield, providing the correct physical normalization.

9 Photon or neutrino signal lead time

If bubble walls in the $SU(3)_c$ scenario propagate at slightly subluminal speeds, any secondary radiation (photons or neutrinos from colored scalar or massive gluons) will arrive earlier than the wall itself. Such particles may thus act as a cosmological “advance warning” of the approaching bubble. We now quantify this delay for a source situated at a distance of 1 billion light years.

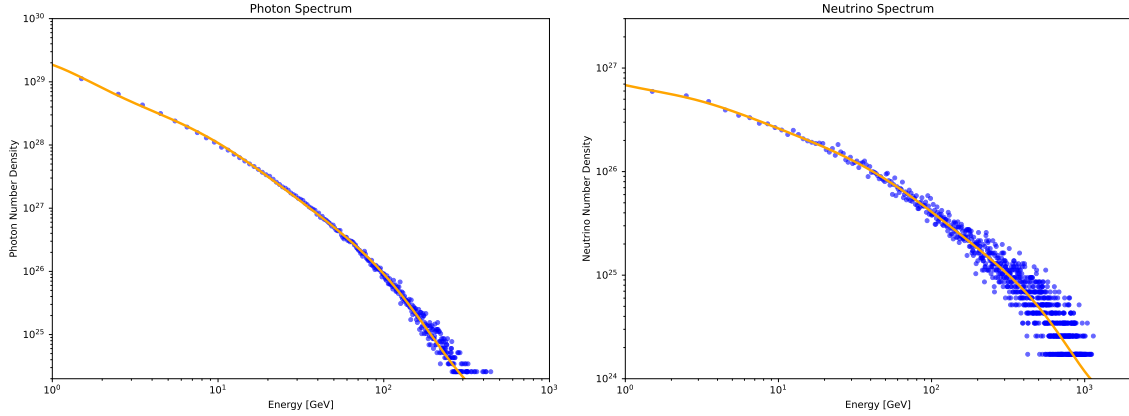


Figure 7. The spectrum of photons and neutrinos generated by decays of 2.5 TeV physical color octet produced near true-vacuum bubbles. The two curves correspond to photons and neutrinos spectra for a terminal wall velocity, characterized by $\delta = 10^{-12}$, respectively, as summarized in Table 4.

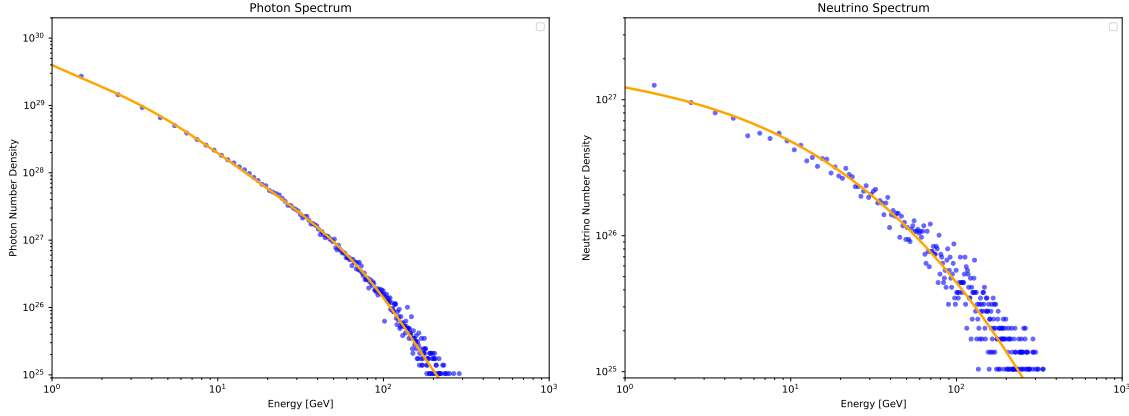


Figure 8. The spectrum of photons and neutrinos generated by decays of 1 TeV massive gluons produced near true-vacuum bubbles. The two curves correspond to photons and neutrinos spectra for a terminal wall velocity, characterized by $\delta = 10^{-12}$, respectively, as summarized in Table 4.

Cosmological inputs and arrival delay For the benchmark estimate considered here, a full cosmological treatment is not necessary. We take a source at a distance

$$D = 10^9 \text{ ly}, \quad (9.1)$$

which corresponds to a modest redshift, $z \simeq 0.07$, in a flat Λ CDM cosmology. At such low redshift, the difference between the exact cosmological result and the flat-space estimate is negligible for our purposes, so we use the Minkowski approximation throughout this subsection. If the bubble wall propagates at speed

$$v = (1 - \delta)c, \quad \delta \ll 1, \quad (9.2)$$

then the arrival delay relative to photons or neutrinos is

$$\Delta t \simeq D \left(\frac{1}{v} - \frac{1}{c} \right) = \frac{\delta}{1 - \delta} \frac{D}{c} \simeq \delta \frac{D}{c}. \quad (9.3)$$

For $D = 10^9$ light years, this gives the lead times listed in Table 5.

Velocity Deficit δ	Distance (ly)	Time Delay
1.0×10^{-10}	1.0×10^9	35 d, 7 h, 23 m, 55.25 s
1.0×10^{-11}	1.0×10^9	3 d, 12 h, 44 m, 23.52 s
1.0×10^{-12}	1.0×10^9	0 d, 8 h, 28 m, 26.35 s

Table 5. Photon/neutrino lead times for bubble walls with subluminal deficits δ created at a distance of 10^9 light years from us, using the flat-space approximation $\Delta t \simeq \delta D/c$. Even for $\delta = 10^{-12}$, the lead time is several hours, while larger deficits extend the warning to days or weeks.

Thus, in the $SU(3)_c$ model, even minuscule velocity deficits can produce noticeable precursor signals. Depending on δ , colored scalar decays into photons or neutrinos could reach observers hours to weeks before the bubble wall, offering a potential advance probe of cosmological first-order transitions.

10 Conclusions

In this work, we investigated the potential cosmological signatures stemming from a catastrophic phase transition in which the strong nuclear force, described by the $SU(3)_c$ gauge symmetry, becomes spontaneously broken. While the $SU(3)_c$ symmetry defines the fundamental structure of our present-day universe and is essential for life as we know it, there is no fundamental principle guaranteeing its eternal persistence. To explore the observational consequences of such an event, we constructed a phenomenological model incorporating a new colored scalar field responsible for the symmetry breaking. The potential of this field facilitates a first-order phase transition, a process driven by the nucleation and expansion of bubbles of true vacuum within the surrounding false vacuum of our current $SU(3)_c$ -symmetric state.

Our analysis focused on the particle production mechanisms triggered by this violent transition. The vacuum mismatch across the bubble walls leads to the abundant production of the new scalar field itself, as well as massive gluons and color octet scalars. We employed event generators to simulate the subsequent decay chains of these primary particles. The final states of these decays were then hadronized using Pythia to obtain the precise spectra of stable particles that would propagate across cosmological distances. Our key finding is that this phase transition would generate a distinct, long-range signature dominated by high-energy photons and neutrinos. Therefore, the detection of a specific, diffuse background of photons and neutrinos, inconsistent with any known astrophysical or cosmological source, could serve as a potential indicator of this profound transformation. Consequently, such an observation might be interpreted not merely as evidence of new physics, but as an empirical signal of a fundamental shift in the laws of nature, a cosmological "doomsday" event that alters the very forces governing the universe.

In the absence of friction, the bubble walls traveling with the speed of light would hit us at the same time as the signal coming from them. However, a bubble almost always travels through some medium, for example plasma if formed in the early universe or inside stars, or through the interstellar and intergalactic gas. Most importantly, a bubble of true vacuum is engulfed in a sea of particles that produces itself. Therefore, it is not unreasonable to expect that the bubble wall will reach a terminal velocity slightly below the speed of light. Even a very modest slowdown when extrapolated over the cosmological distances may give us days, months, or even years of warning time before the wall hits us. For illustration, we presented neutrino and photon spectra produced only up to the time when the terminal velocity is reached for a conservative value of the friction coefficient. So if we ever measure spectra like in Fig. 7 and 8, they might represent signals of the doomsday. In addition to the particle production from vacuum mismatch which halts upon reaching terminal velocity, thermal particle production will continue due to the substantial energy dissipated into the environment via friction. We incorporated thermal particle production sourced by frictional dissipation behind the wall and showed that, for the benchmark scenarios considered here, this channel can dominate over the direct vacuum-mismatch contribution by many orders of magnitude.

We note that throughout the paper we used a fiducial value for the energy scale of the phase transition of 1 TeV. However, any other value can be used, as long as we are not obviously violating any observational constraints. While the energy scale might be high, the strength of the phase transition (i.e. the difference between the vacua) must be small so that most of the universe is still in the false vacuum today with just a few bubbles here and there. We thus call such phase transitions - late time phase transitions.

Acknowledgments

The authors are grateful to Jure Zupan, D.C. Dai and Manuel Szewc for carefully reviewing the manuscript and for their valuable comments and suggestions. AS and DS are partially supported by the U.S. National Science Foundation, under the Grant No. PHY-2310363. AS is also supported by the Grant No. NSF OAC-2417682. L.C.R. W is supported by the U.S. Department of Energy grant DE-SC0011784.

A Appendix A: Symmetry breaking patterns from the adjoint potential

In this appendix we expand upon the discussion of the scalar potential presented in the Model section [see 2] of the manuscript. Our goal is to analyze in detail how the vacuum alignment of an $SU(3)_c$ adjoint Higgs determines the residual gauge symmetry, and to count the number of massless and massive gluons in each case. We emphasize the role of the cubic invariant, which lifts the angular degeneracy present in the purely quadratic-plus-quartic potential and selects the $U(2)$ -type vacuum alignment relevant for the main text.

Lagrangian and potential

The gauge–scalar sector is given by

$$\mathcal{L} = -\frac{1}{2}\text{Tr}F_{\mu\nu}F^{\mu\nu} + \frac{1}{2}\text{Tr}(D_\mu\Phi)(D^\mu\Phi) - V(\Phi), \quad (\text{A.1})$$

where

$$F_{\mu\nu} = \partial_\mu A_\nu - \partial_\nu A_\mu + ig[A_\mu, A_\nu], \quad D_\mu\Phi = \partial_\mu\Phi + ig[A_\mu, \Phi]. \quad (\text{A.2})$$

The scalar potential is

$$V(\Phi) = \frac{\mu^2}{4}\text{Tr}(\Phi^2) + \frac{\lambda_1}{16}(\text{Tr}\Phi^2)^2 + \frac{\lambda_2}{6}\text{Tr}(\Phi^3) + V_0, \quad \lambda_1 > 0, \quad (\text{A.3})$$

with the constant V_0 set to zero henceforth.

Diagonal VEV and two–variable reduction

We parameterize the vacuum as

$$\langle\Phi\rangle = v = \text{diag}(a, b, c), \quad a + b + c = 0. \quad (\text{A.4})$$

The invariants become

$$\text{Tr}(v^2) = a^2 + b^2 + c^2 =: S_2, \quad (\text{A.5})$$

$$\text{Tr}(v^3) = a^3 + b^3 + c^3 = 3abc, \quad (\text{A.6})$$

so the potential on the VEV subspace reads

$$V(v) = \frac{\mu^2}{4}(a^2 + b^2 + c^2) + \frac{\lambda_1}{16}(a^2 + b^2 + c^2)^2 + \frac{\lambda_2}{2}abc. \quad (\text{A.7})$$

Eliminating $c = -(a + b)$ and defining

$$Q := a^2 + b^2 + ab \quad (\Rightarrow S_2 = 2Q), \quad abc = -ab(a + b), \quad (\text{A.8})$$

we obtain the convenient two–variable form

$$V(a, b) = \frac{\mu^2}{2}Q + \frac{\lambda_1}{4}Q^2 - \frac{\lambda_2}{2}ab(a + b). \quad (\text{A.9})$$

Case I: cubic present ($\lambda_2 \neq 0$) $\Rightarrow U(2)$

From (A.9),

$$\frac{\partial V}{\partial a} = \left(\frac{\mu^2}{2} + \frac{\lambda_1}{2}Q\right)(2a+b) - \frac{\lambda_2}{2}b(2a+b) = 0, \quad (\text{A.10})$$

$$\frac{\partial V}{\partial b} = \left(\frac{\mu^2}{2} + \frac{\lambda_1}{2}Q\right)(2b+a) - \frac{\lambda_2}{2}a(2b+a) = 0. \quad (\text{A.11})$$

Equivalently, after multiplying by 2, these may be written as

$$(2a + b)(\mu^2 + \lambda_1 Q - \lambda_2 b) = 0, \quad (\text{A.10}')$$

$$(2b + a)(\mu^2 + \lambda_1 Q - \lambda_2 a) = 0. \quad (\text{A.11}')$$

Subtracting the two equations gives a factorized condition relating the angular variables. In particular, there exists a nontrivial stationary branch with

$$a = b, \quad c = -2a, \quad (\text{A.10})$$

for which two eigenvalues coincide. This is precisely the vacuum alignment relevant to the benchmark used in the main text, and it leads to the breaking pattern

$$SU(3) \longrightarrow U(2) \simeq SU(2) \times U(1), \quad (\text{A.11})$$

with

$$4 \text{ massless gluons}, \quad 4 \text{ massive gluons}. \quad (\text{A.12})$$

Case II: cubic absent ($\lambda_2 = 0$) $\Rightarrow U(1) \times U(1)$ (for $\mu^2 < 0$)

With $\lambda_2 = 0$ the adjoint potential reads

$$V(a, b) = \frac{\mu^2}{2} Q + \frac{\lambda_1}{4} Q^2, \quad Q \equiv a^2 + b^2 + ab, \quad (\text{A.13})$$

where we take $\lambda_1 > 0$ so that the potential is bounded from below. The stationarity conditions are

$$\frac{\partial V}{\partial a} = (2a+b) [\mu^2 + 2\lambda_1 Q] = 0, \quad (\text{A.14})$$

$$\frac{\partial V}{\partial b} = (2b+a) [\mu^2 + 2\lambda_1 Q] = 0. \quad (\text{A.15})$$

On the sign of μ^2 . If $\mu^2 > 0$, then $V = \frac{\mu^2}{2} Q + \frac{\lambda_1}{4} Q^2 \geq 0$ with $V = 0$ only at $Q = 0 \Rightarrow a = b = 0$. In this case the *only* local minimum is the trivial vacuum $a = b = 0$, and the full $SU(3)$ remains unbroken. Thus nontrivial vacua arise *only if* $\mu^2 < 0$.

Nontrivial vacua for $\mu^2 < 0$. Adding Eqs. (A.14) and (A.15) gives

$$3(a+b) [\mu^2 + 2\lambda_1 Q] = 0. \quad (\text{A.16})$$

For $\mu^2 < 0$, the minimum is determined by the radial condition

$$\mu^2 + 2\lambda_1 Q = 0 \quad \Longrightarrow \quad Q = -\frac{\mu^2}{2\lambda_1}, \quad (\text{A.17})$$

which fixes only the radius in (a, b) -space, while the angular direction remains undetermined. It is often convenient to introduce the angular ratio

$$r \equiv \frac{b}{a}. \quad (\text{A.18})$$

For generic $r \neq 1, -2$, the three eigenvalues are all distinct. The special case

$$a + b = 0 \quad \Rightarrow \quad b = -a \quad (\text{A.19})$$

is simply one representative point on the same vacuum manifold; in this case $Q = a^2$ and the radial condition becomes

$$\mu^2 + 2\lambda_1 a^2 = 0 \quad \Longrightarrow \quad a^2 = -\frac{\mu^2}{2\lambda_1}, \quad (\mu^2 < 0). \quad (\text{A.20})$$

Potential choice	Vacuum alignment	Unbroken H	Massive/Massless gluons	Massive/Massless scalars
$\lambda_2 \neq 0$ (cubic present)	$a = b \neq c$	$U(2)$	4 massive, 4 massless	4 massive, 4 eaten
$\lambda_2 = 0, \mu^2 > 0$	$a = b = 0$ (trivial)	$SU(3)$	0 massive, 8 massless	8 massive, 0 eaten
$\lambda_2 = 0, \mu^2 < 0$	$a \neq b \neq c$ (generic)	$U(1) \times U(1)$	6 massive, 2 massless	2 massive, 6 eaten

Table 6. Summary of vacuum alignments and residual gauge symmetries arising from the adjoint scalar potential of $SU(3)_c$, together with the associated gluon and scalar mass spectra. The scalar counts refer to the adjoint scalar degrees of freedom after symmetry breaking, with Goldstone modes counted as eaten by the corresponding massive gauge bosons. The table serves as a compact reference for the symmetry breaking patterns discussed throughout the paper.

Residual symmetry and gauge–boson masses

Let the three adjoint eigenvalues be (a, b, c) with $a+b+c = 0$ (traceless). The tree–level gauge masses follow from the adjoint covariant derivative. Up to the normalization convention chosen for the adjoint vacuum expectation value, the off–diagonal gauge–boson masses scale as

$$m^2(E_{ij}) \propto g^2 (a_i - a_j)^2 \quad (i \neq j), \quad m^2(\text{Cartan}) = 0, \quad (\text{A.21})$$

where the six off–diagonal generators E_{ij} ($i \neq j$) acquire masses proportional to the squared differences of the adjoint eigenvalues, while the two diagonal (Cartan) generators remain massless.

For *generic, nondegenerate* eigenvalues ($a \neq b \neq c$) one obtains the breaking pattern

$$SU(3) \longrightarrow U(1) \times U(1), \quad 6 \text{ massive gluons, } 2 \text{ massless (Cartan) gluons.}$$

This situation corresponds to the generic angular branch with $r \neq 1, -2$, and also includes the representative point $b = -a$ with $c = -(a+b) = 0$, provided all (a, b, c) are pairwise distinct. In the special degenerate cases $r = 1$ or $r = -2$, two eigenvalues coincide and the symmetry is restored to

$$SU(3) \longrightarrow U(2),$$

yielding 4 massive and 4 massless gluons.

Order of the transition. The breaking pattern and the order of the transition are logically distinct. For $\lambda_2 \neq 0$, the cubic invariant $\text{Tr}(\Phi^3)$ generically creates a barrier between the symmetric and broken phases along the order–parameter direction, yielding a *first-order* transition (thin-wall/bounce applies). By contrast, for $\lambda_2 = 0$ the potential reduces to

$$V = \frac{\mu^2}{2}Q + \frac{\lambda_1}{4}Q^2, \quad Q = a^2 + b^2 + ab,$$

with $\lambda_1 > 0$. There is no tree–level barrier: as μ^2 passes through zero, the minimum moves continuously from $Q = 0$ to $Q = -\mu^2/(2\lambda_1)$. Thus, at tree level the $\lambda_2 = 0$ branch is second order (continuous). A generic adjoint vacuum expectation value (VEV) breaks $SU(3) \rightarrow U(1) \times U(1)$, while along the degenerate alignment $a = b$ the unbroken subgroup is restored to $U(2)$.

When the adjoint scalar acquires a VEV aligned with the eighth Gell–Mann generator, the color group breaks as $SU(3)_c \rightarrow U(2) \simeq SU(2)_{rg} \times U(1)_X$, where the unbroken generators $\{T_{1,2,3}, T_8\}$ act block-diagonally on the (r, g) and b color directions. As a result, the red–green sector forms an $SU(2)_{rg}$ doublet while the blue quark is an $SU(2)$ singlet carrying only $U(1)_X$ charge. The four off-diagonal generators $\{T_{4-7}\}$ do not commute with T_8 , so their gauge bosons acquire masses of order $M_g \sim g_s \psi_0 \sim \text{TeV}$ and decouple from infrared physics. Below the breaking scale the couplings of the unbroken subgroup run differently: $SU(2)_{rg}$ remains asymptotically free and becomes confining at low energies, while the Abelian $U(1)_X$ coupling weakens like QED. Consequently, the dynamics inside the broken-color phase resemble a confining two-color gauge theory coupled to a weak long-range $U(1)$: (r, g) quarks form $SU(2)$ mesons and diquark baryons, whereas blue quarks are singlets under the confining $SU(2)_{rg}$ factor, so the usual three-color baryon picture is no longer operative in the broken phase. The massive gluons do not bind via massive-gluon exchange (which is exponentially suppressed), but they can form bound states because they remain charged under the unbroken $SU(2)_{rg} \times U(1)_X$ subgroup and therefore continue to participate in the residual confining $SU(2)$ dynamics. In summary, the broken phase realizes a rich $U(2)$ gauge structure with qualitatively new spectroscopy, modified running, and non-standard hadronization patterns; a detailed quantitative analysis of these features, including spectrum, potentials, and RG flows, will be developed in a follow-up paper.

B Appendix B: Quartic trace identity for $SU(3)$ adjoint fields

We establish the relation

$$(\text{Tr } M^2)^2 = 2 \text{Tr } M^4, \quad (\text{B.1})$$

for $M = B_a T^a$, where T^a are the $SU(3)$ generators in the fundamental, normalized as

$$\text{Tr}(T^a T^b) = \frac{1}{2} \delta^{ab}, \quad a, b = 1, \dots, 8. \quad (\text{B.2})$$

This identity is specific to traceless 3×3 matrices (hence to $SU(3)$) and will be used to reduce quartic adjoint invariants to a single structure.

Cayley–Hamilton proof

For any traceless 3×3 matrix A the Cayley–Hamilton theorem implies

$$A^3 - \frac{1}{2} \text{Tr}(A^2) A - (\det A) \mathbf{1} = 0. \quad (\text{B.3})$$

Multiplying (B.3) by A and taking the trace gives

$$\text{Tr}(A^4) = \frac{1}{2} (\text{Tr } A^2)^2. \quad (\text{B.4})$$

Specializing to $A = M$ directly leads to

$$(\text{Tr } M^2)^2 = 2 \text{Tr } M^4, \quad (\text{B.5})$$

which is the desired identity (B.1).

Group–theory proof

Using the product decomposition

$$T^a T^b = \frac{1}{2N} \delta^{ab} \mathbb{1} + \frac{1}{2} (d^{abc} + i f^{abc}) T^c, \quad (N = 3), \quad (\text{B.6})$$

and the fact that $B_a B_b f^{abc} = 0$, one finds

$$M^2 = \frac{B^2}{6} \mathbb{1} + \frac{1}{2} S^c T^c, \quad B^2 \equiv B_a B_a, \quad S^c \equiv d^{abc} B_a B_b. \quad (\text{B.7})$$

Squaring and tracing gives

$$\text{Tr } M^4 = \frac{B^4}{12} + \frac{1}{8} S^2, \quad S^2 \equiv S^c S^c. \quad (\text{B.8})$$

For $SU(3)$ the dd identity

$$d^{abe} d^{cde} + d^{ace} d^{bde} + d^{ade} d^{bce} = \frac{1}{3} (\delta^{ab} \delta^{cd} + \delta^{ac} \delta^{bd} + \delta^{ad} \delta^{bc}) \quad (\text{B.9})$$

implies, upon contraction with $B_a B_b B_c B_d$, that

$$S^2 = \frac{1}{3} B^4. \quad (\text{B.10})$$

Substituting (B.10) into (B.8) yields

$$\text{Tr } M^4 = \frac{1}{8} B^4. \quad (\text{B.11})$$

Since $\text{Tr } M^2 = \frac{1}{2} B^2$, it follows that

$$(\text{Tr } M^2)^2 = \frac{1}{4} B^4 = 2 \text{Tr } M^4, \quad (\text{B.12})$$

confirming the result.

Consequence for quartic adjoint invariants

Because $\text{Tr } M^4 = \frac{1}{2} (\text{Tr } M^2)^2$ in $SU(3)$, any renormalizable quartic built from one adjoint reduces to a single effective coupling. In particular,

$$g_1 (\text{Tr } M^2)^2 + g_2 \text{Tr } (M^4) = \left(g_1 + \frac{1}{2} g_2 \right) (\text{Tr } M^2)^2. \quad (\text{B.13})$$

Thus there is only one independent four-point coupling constant for adjoint $SU(3)$ fields at dimension four.

C Appendix C: Particle production from a massive vector field

In our model the cubic term in the adjoint potential aligns the vacuum expectation value along

$$v \propto \text{diag}(1, 1, -2), \quad (\text{C.1})$$

so that the unbroken subgroup is $U(2)$. The gauge spectrum therefore contains four massive gluons and four massless gluons. The four massive states acquire their longitudinal polarizations by eating the corresponding Goldstone scalars, while the gauge bosons associated with the unbroken $U(2)$ subgroup remain massless.

We work in unitary (Proca) gauge. For the purposes of the present analysis, we retain only the two transverse polarizations of each massive gluon. A proper treatment of the longitudinal modes requires a coupled scalar–vector analysis across the bubble wall and is left for future work.

In Euclidean time $\tilde{\tau}$, each transverse mode satisfies

$$\partial_{\tilde{\tau}}^2 g_i^a(\tilde{\tau}, \mathbf{x}) + \nabla^2 g_i^a(\tilde{\tau}, \mathbf{x}) - m_g^2(\tilde{\tau}) g_i^a(\tilde{\tau}, \mathbf{x}) = 0, \quad (\text{C.2})$$

with a sudden mass jump at $\tilde{\tau} = \tilde{\tau}^*$,

$$m_g(\tilde{\tau}) = \begin{cases} M_g, & \tilde{\tau} < \tilde{\tau}^*, \\ \mu_g, & \tilde{\tau} > \tilde{\tau}^*. \end{cases} \quad (\text{C.3})$$

In our case the gluons are massless in the false vacuum and massive in the true vacuum, so

$$M_g = 0, \quad \mu_g \simeq 1 \text{ TeV}. \quad (\text{C.4})$$

Decomposing into momentum modes and transverse polarization vectors $\epsilon_i^{(\lambda)}$ gives

$$g_i^a(\tilde{\tau}, \mathbf{x}) = \sum_{\lambda=1}^2 \int \frac{d^3 k}{(2\pi)^3} \epsilon_i^{(\lambda)}(\mathbf{k}) g_k^{a(\lambda)}(\tilde{\tau}) e^{i\mathbf{k}\cdot\mathbf{x}}, \quad (\text{C.5})$$

where the sum runs only over the two transverse polarizations. The time-dependent mode function then obeys

$$g_k''(\tilde{\tau}) + [k^2 + m_g^2(\tilde{\tau})] g_k(\tilde{\tau}) = 0. \quad (\text{C.6})$$

The transverse mode functions are matched in exactly the same way as in the main text for the scalar case, now applied to each transverse polarization of the massive gluon. The general solution is

$$g_k(\tilde{\tau}) = \begin{cases} e^{\omega_- \tilde{\tau}}, & \tilde{\tau} < \tilde{\tau}^*, \\ A_k e^{\omega_+ \tilde{\tau}} + B_k e^{-\omega_+ \tilde{\tau}}, & \tilde{\tau} > \tilde{\tau}^*, \end{cases} \quad (\text{C.7})$$

where

$$\omega_- = \sqrt{k^2 + M_g^2}, \quad \omega_+ = \sqrt{k^2 + \mu_g^2}. \quad (\text{C.8})$$

Requiring continuity of both g_k and $\partial_{\tilde{\tau}} g_k$ at $\tilde{\tau} = \tilde{\tau}^*$ yields

$$A_k = \frac{1}{2\omega_+} (\omega_+ + \omega_-) e^{-(\omega_+ - \omega_-)\tilde{\tau}^*}, \quad B_k = \frac{1}{2\omega_+} (\omega_+ - \omega_-) e^{(\omega_+ + \omega_-)\tilde{\tau}^*}. \quad (\text{C.9})$$

As in the main text, we set

$$\tilde{\tau}^* = -R_0, \quad (\text{C.10})$$

with R_0 the nucleation radius of the bubble.

The particle-production spectrum per mode is then obtained from the corresponding Bogoliubov transform,

$$N_k = \frac{B_k^2}{A_k^2 - B_k^2} = \left[\frac{(\omega_+ + \omega_-)^2}{(\omega_+ - \omega_-)^2} e^{4\omega_+ R_0} - 1 \right]^{-1}. \quad (\text{C.11})$$

This expression applies to each transverse polarization separately. In the phenomenological analysis in the main text, we retain only the two transverse polarizations of each of the four massive gluons. The total transverse gluon contribution is therefore obtained by summing over these eight transverse modes.

D Appendix D: Derivation of $\Gamma(G \rightarrow q\bar{q})$

We compute the tree-level partial width for a massive color-octet vector boson g_μ^a (“massive gluon”) of mass M_g decaying into a Dirac quark of mass m_q and its antiquark via the QCD-like interaction.

Interaction and amplitude

The interaction Lagrangian is

$$\mathcal{L}_{\text{int}} = g_s \bar{q}_i \gamma^\mu T_{ij}^a q_j g_\mu^a, \quad (\text{D.1})$$

with T^a the SU(3) generators in the fundamental, normalized by $\text{Tr}[T^a T^b] = T(R) \delta^{ab}$, $T(R) = \frac{1}{2}$. For a fixed adjoint color a , the decay amplitude is

$$\mathcal{M} = g_s \bar{u}_i(p) \gamma^\mu T_{ij}^a v_j(p') \varepsilon_\mu(k), \quad k = p + p', \quad k^2 = M_g^2. \quad (\text{D.2})$$

Spin, polarization, and color algebra

Now averaging over the *three* initial polarizations of a massive vector (Proca field) and summing over final spins and colors, we get

$$|\overline{\mathcal{M}}|^2 = \frac{1}{3} \sum_{\text{spins, colors}} \mathcal{M} \mathcal{M}^\dagger. \quad (\text{D.3})$$

Using the Proca completeness relation for the polarization sum,

$$\sum_{\lambda=1}^3 \varepsilon_\mu^{(\lambda)}(k) \varepsilon_\nu^{(\lambda)*}(k) = -g_{\mu\nu} + \frac{k_\mu k_\nu}{M_g^2}, \quad (\text{D.4})$$

and current conservation for equal-mass external spinors,

$$k_\mu \bar{u}(p) \gamma^\mu v(p') = \bar{u}(p) (\not{p} + \not{p}') v(p') = \bar{u}(p) (m_q - m_q) v(p') = 0, \quad (\text{D.5})$$

the $k_\mu k_\nu / M_g^2$ term in (D.4) drops out, so effectively we can replace $\sum_\lambda \varepsilon_\mu \varepsilon_\nu^* \rightarrow -g_{\mu\nu}$.

Now we sum over the final colors i, j but we keep the initial a fixed:

$$\sum_{i,j} T_{ij}^a T_{ji}^a = \text{Tr}[T^a T^a] = T(R) = \frac{1}{2}. \quad (\text{D.6})$$

For the spin sums we use completeness, $\sum_s u(p)\bar{u}(p) = \not{p} + m_q$ and $\sum_s v(p')\bar{v}(p') = \not{p}' - m_q$, to obtain the Dirac trace

$$\begin{aligned} \sum_{\text{spins}} \bar{u}(p)\gamma^\mu v(p') \bar{v}(p')\gamma^\nu u(p) &= \text{Tr}[(\not{p} + m_q)\gamma^\mu (\not{p}' - m_q)\gamma^\nu] \\ &= 4\left(p^\mu p'^\nu + p^\nu p'^\mu - g^{\mu\nu}(p\cdot p' + m_q^2)\right). \end{aligned} \quad (\text{D.7})$$

Contracting with $-g_{\mu\nu}$ from the polarization sum gives

$$\begin{aligned} -g_{\mu\nu} \text{Tr}[\dots] &= 4(-p\cdot p' - p\cdot p' + 4(p\cdot p' + m_q^2)) \\ &= 8(p\cdot p' + 2m_q^2). \end{aligned} \quad (\text{D.8})$$

Putting the pieces together,

$$|\overline{\mathcal{M}}|^2 = \frac{1}{3}g_s^2 \text{Tr}[T^a T^a] \left[8(p\cdot p' + 2m_q^2)\right] = \frac{4}{3}g_s^2 (p\cdot p' + 2m_q^2), \quad (\text{D.9})$$

since $\text{Tr}[T^a T^a] = 1/2$ for fixed a .

It is often convenient to express $p\cdot p'$ in terms of invariants. Using $(p+p')^2 = M_g^2 = 2m_q^2 + 2p\cdot p'$, we have $p\cdot p' = \frac{1}{2}(M_g^2 - 2m_q^2)$, so that

$$|\overline{\mathcal{M}}|^2 = \frac{2}{3}g_s^2 (M_g^2 + 2m_q^2). \quad (\text{D.10})$$

Two-body phase space

For a $1 \rightarrow 2$ decay into equal masses, the integrated two-body phase space is

$$\int d\Phi_2 = \frac{\beta}{8\pi}, \quad \beta \equiv \sqrt{1 - \frac{4m_q^2}{M_g^2}}, \quad (\text{D.11})$$

and the standard decay-width formula reads

$$\Gamma = \frac{1}{2M_g} |\overline{\mathcal{M}}|^2 \int d\Phi_2 = \frac{\beta}{16\pi M_g} |\overline{\mathcal{M}}|^2. \quad (\text{D.12})$$

Final result

Substituting (D.10) into (D.12) and using $g_s^2 = 4\pi\alpha_s$, we obtain

$$\begin{aligned} \Gamma(g \rightarrow q\bar{q}) &= \frac{\beta}{16\pi M_g} \frac{2}{3} g_s^2 (M_g^2 + 2m_q^2) \\ &= \frac{4\pi\alpha_s}{24\pi} M_g \left(1 + 2\frac{m_q^2}{M_g^2}\right) \beta \\ &= \frac{\alpha_s}{6} M_g \left(1 + 2\frac{m_q^2}{M_g^2}\right) \sqrt{1 - \frac{4m_q^2}{M_g^2}}. \end{aligned} \quad (\text{D.13})$$

This formula is for a fixed adjoint color a (no average over a). It reduces to $\Gamma = \frac{\alpha_s}{6} M_g$ for massless quarks and vanishes at threshold $M_g = 2m_q$.

E Appendix E: Derivation of $\Gamma(G_H \rightarrow q\bar{q})$

In this appendix we derive the tree-level partial width for a physical adjoint scalar component G_H^a of mass M_{G_H} decaying into a Dirac quark of mass m_q and its antiquark. Since the minimal broken-color model written in the main text does not by itself generate a direct scalar–quark Yukawa interaction, we assume here an effective coupling of the form

$$\mathcal{L}_{\text{int}} = -y_q G_H^a \bar{q}_i T_{ij}^a q_j, \quad (\text{E.1})$$

where T^a are the $SU(3)$ generators in the fundamental representation, normalized as [62, 63]

$$\text{Tr}(T^a T^b) = T(R) \delta^{ab}, \quad T(R) = \frac{1}{2}. \quad (\text{E.2})$$

This effective interaction may be viewed as a phenomenological parametrization of the coupling of a given physical scalar mode to quarks after symmetry breaking. In applications one may further choose, for example, a normalization inspired from minimal-flavor-violation $y_q = \eta_q m_q/v$, but for the derivation below we keep y_q general.

Interaction and amplitude

For a fixed adjoint color a , the decay process

$$G_H^a(k) \rightarrow q_i(p) \bar{q}_j(p'), \quad k = p + p', \quad k^2 = M_{G_H}^2, \quad (\text{E.3})$$

has tree-level amplitude

$$\mathcal{M} = y_q \bar{u}_i(p) T_{ij}^a v_j(p'). \quad (\text{E.4})$$

Since the initial particle is a scalar, there is no spin or polarization average.

Spin and color algebra

Summing over the final spins and colors, we obtain

$$\sum_{\text{spins, colors}} |\mathcal{M}|^2 = y_q^2 \sum_{\text{spins, colors}} \bar{u}_i(p) T_{ij}^a v_j(p') \bar{v}_{j'}(p') T_{j'i}^a u_{i'}(p). \quad (\text{E.5})$$

The color sum is straightforward:

$$\sum_{i,j} T_{ij}^a T_{ji}^a = \text{Tr}(T^a T^a) = T(R) = \frac{1}{2}. \quad (\text{E.6})$$

For the spin sums we use

$$\sum_s u(p) \bar{u}(p) = \not{p} + m_q, \quad \sum_s v(p') \bar{v}(p') = \not{p}' - m_q, \quad (\text{E.7})$$

which gives

$$\begin{aligned} \sum_{\text{spins}} \bar{u}(p) v(p') \bar{v}(p') u(p) &= \text{Tr}[(\not{p} + m_q)(\not{p}' - m_q)] \\ &= 4(p \cdot p' - m_q^2). \end{aligned} \quad (\text{E.8})$$

Combining the spin and color factors, we get

$$\sum |\mathcal{M}|^2 = y_q^2 \text{Tr}(T^a T^a) 4(p \cdot p' - m_q^2) = 2y_q^2(p \cdot p' - m_q^2). \quad (\text{E.9})$$

It is useful to rewrite this in terms of invariants. Since

$$(p + p')^2 = M_{G_H}^2 = 2m_q^2 + 2p \cdot p', \quad (\text{E.10})$$

we have

$$p \cdot p' = \frac{M_{G_H}^2 - 2m_q^2}{2}, \quad (\text{E.11})$$

and therefore

$$p \cdot p' - m_q^2 = \frac{M_{G_H}^2 - 4m_q^2}{2}. \quad (\text{E.12})$$

The squared matrix element then becomes

$$\sum |\mathcal{M}|^2 = y_q^2 (M_{G_H}^2 - 4m_q^2). \quad (\text{E.13})$$

Two-body phase space

For a scalar decaying into two equal-mass fermions, the integrated two-body phase space is

$$\int d\Phi_2 = \frac{\beta_q}{8\pi}, \quad \beta_q \equiv \sqrt{1 - \frac{4m_q^2}{M_{G_H}^2}}. \quad (\text{E.14})$$

The standard decay-width formula is therefore

$$\Gamma = \frac{1}{2M_{G_H}} \sum |\mathcal{M}|^2 \int d\Phi_2 = \frac{\beta_q}{16\pi M_{G_H}} \sum |\mathcal{M}|^2. \quad (\text{E.15})$$

Substituting (E.13), we obtain

$$\Gamma(G_H^a \rightarrow q\bar{q}) = \frac{\beta_q}{16\pi M_{G_H}} y_q^2 (M_{G_H}^2 - 4m_q^2). \quad (\text{E.16})$$

Using

$$M_{G_H}^2 - 4m_q^2 = M_{G_H}^2 \beta_q^2, \quad (\text{E.17})$$

the result simplifies to

$$\Gamma(G_H^a \rightarrow q\bar{q}) = \frac{y_q^2 M_{G_H}}{16\pi} \beta_q^3. \quad (\text{E.18})$$

Final result

The tree-level partial width for a fixed adjoint scalar component G_H^a decaying to a quark–antiquark pair is therefore

$$\Gamma(G_H^a \rightarrow q\bar{q}) = \frac{y_q^2 M_{G_H}}{16\pi} \left(1 - \frac{4m_q^2}{M_{G_H}^2}\right)^{3/2}. \quad (\text{E.19})$$

If one adopts the phenomenological normalization

$$y_q = \eta_q \frac{m_q}{v}, \quad (\text{E.20})$$

with $v = 246$ GeV, the width may be written as

$$\Gamma(G_H^a \rightarrow q\bar{q}) = \frac{\eta_q^2 m_q^2 M_{G_H}}{16\pi v^2} \left(1 - \frac{4m_q^2}{M_{G_H}^2}\right)^{3/2}. \quad (\text{E.21})$$

This formula is for a fixed adjoint index a and vanishes at threshold $M_{G_H} = 2m_q$.

F Appendix F: Derivation of $\Gamma(G_H \rightarrow gg)$

In this appendix we derive the one-loop partial width for a physical adjoint scalar component G_H^a of mass M_{G_H} decaying into two gluons through quark triangle diagrams. We again assume the effective Yukawa interaction

$$\mathcal{L}_{\text{int}} = -y_q G_H^a \bar{q}_i T_{ij}^a q_j, \quad (\text{F.1})$$

together with the standard QCD coupling

$$\mathcal{L}_{\text{QCD}} = g_s \bar{q}_i \gamma^\mu T_{ij}^b q_j g_\mu^b. \quad (\text{F.2})$$

The decay $G_H^a \rightarrow g^b g^c$ then proceeds through the usual quark triangle, summed over the quark flavors circulating in the loop [61, 64].

Color structure of the triangle amplitude

For a fixed incoming scalar color a and outgoing gluon colors b, c , the two triangle orderings produce the color factor

$$\text{Tr}(T^a T^b T^c) + \text{Tr}(T^a T^c T^b) = \text{Tr}(T^a \{T^b, T^c\}). \quad (\text{F.3})$$

Using

$$\{T^b, T^c\} = \frac{1}{3} \delta^{bc} \mathbb{1} + d^{bcd} T^d, \quad (\text{F.4})$$

together with $\text{Tr}(T^a) = 0$, one obtains

$$\text{Tr}(T^a \{T^b, T^c\}) = d^{bcd} \text{Tr}(T^a T^d) = \frac{1}{2} d^{abc}. \quad (\text{F.5})$$

Thus the decay amplitude is proportional to the totally symmetric $SU(3)$ tensor d^{abc} , as expected for a CP-even scalar coupled to two gauge bosons.

General form of the amplitude

Gauge invariance fixes the Lorentz structure of the on-shell amplitude to be transverse with respect to both external gluon momenta. It is therefore convenient to write the amplitude as

$$i\mathcal{M}_{\mu\nu}^{abc} = i d^{abc} C_{GH} \left[(p_1 \cdot p_2) g_{\mu\nu} - p_{2\mu} p_{1\nu} \right], \quad (\text{F.6})$$

where $p_1^2 = p_2^2 = 0$ and $(p_1 + p_2)^2 = M_{GH}^2$. The loop coefficient C_{GH} contains the quark masses, Yukawa couplings, and the standard scalar triangle form factor. Summing over all quark flavors in the loop, one finds

$$C_{GH} = \frac{\alpha_s}{6\pi} \sum_q \frac{y_q}{m_q} F_{1/2}(\tau_q), \quad \tau_q \equiv \frac{4m_q^2}{M_{GH}^2}. \quad (\text{F.7})$$

Here $F_{1/2}(\tau)$ is the usual spin- $\frac{1}{2}$ scalar loop form factor. A convenient representation is

$$F_{1/2}(\tau) = \frac{3}{2\tau^2} \left[\tau + (\tau - 1)f(\tau) \right], \quad (\text{F.8})$$

with

$$f(\tau) = \begin{cases} \arcsin^2(1/\sqrt{\tau}), & \tau \geq 1, \\ -\frac{1}{4} \left[\ln \left(\frac{1 + \sqrt{1 - \tau}}{1 - \sqrt{1 - \tau}} \right) - i\pi \right]^2, & \tau < 1. \end{cases} \quad (\text{F.9})$$

This normalization is such that $F_{1/2}(\tau) \rightarrow 1$ in the heavy-fermion limit $\tau \rightarrow \infty$.

Polarization and color sums

To obtain the squared amplitude we sum over the two transverse polarizations of each final-state gluon and over the final-state colors b, c . Defining

$$T_{\mu\nu} \equiv (p_1 \cdot p_2) g_{\mu\nu} - p_{2\mu} p_{1\nu}, \quad (\text{F.10})$$

the squared matrix element becomes

$$\sum |\mathcal{M}|^2 = \sum_{b,c,\text{pol}} d^{abc} d^{abc} |C_{GH}|^2 T_{\mu\nu} T^{\mu\nu}. \quad (\text{F.11})$$

For on-shell massless gluons,

$$p_1^2 = p_2^2 = 0, \quad p_1 \cdot p_2 = \frac{M_{GH}^2}{2}, \quad (\text{F.12})$$

and the polarization sum yields

$$\sum_{\text{pol}} T_{\mu\nu} T^{\mu\nu} = 2(p_1 \cdot p_2)^2 = \frac{M_{GH}^4}{2}. \quad (\text{F.13})$$

For a fixed initial adjoint index a , the color identity

$$\sum_{b,c} d^{abc} d^{abc} = \frac{5}{3} \quad (\text{F.14})$$

then gives

$$\sum |\mathcal{M}|^2 = \frac{5}{3} |C_{GH}|^2 \frac{M_{GH}^4}{2}. \quad (\text{F.15})$$

Two-body phase space

The final state consists of two identical massless bosons. The integrated two-body phase space therefore gives

$$\Gamma = \frac{1}{32\pi M_{G_H}} \sum |\mathcal{M}|^2. \quad (\text{F.16})$$

Substituting the expression above, one obtains

$$\Gamma(G_H^a \rightarrow gg) = \frac{1}{32\pi M_{G_H}} \frac{5}{3} |C_{G_H}|^2 \frac{M_{G_H}^4}{2} = \frac{5M_{G_H}^3}{192\pi} |C_{G_H}|^2. \quad (\text{F.17})$$

Inserting

$$C_{G_H} = \frac{\alpha_s}{6\pi} \sum_q \frac{y_q}{m_q} F_{1/2}(\tau_q), \quad (\text{F.18})$$

we arrive at the final result

$$\Gamma(G_H^a \rightarrow gg) = \frac{5\alpha_s^2 M_{G_H}^3}{6912\pi^3} \left| \sum_q \frac{y_q}{m_q} F_{1/2}(\tau_q) \right|^2. \quad (\text{F.19})$$

Phenomenological normalization

If the effective Yukawa coupling is written as

$$y_q = \eta_q \frac{m_q}{v}, \quad v = 246 \text{ GeV}, \quad (\text{F.20})$$

then the width takes the form

$$\Gamma(G_H^a \rightarrow gg) = \frac{5\alpha_s^2 M_{G_H}^3}{6912\pi^3 v^2} \left| \sum_q \eta_q F_{1/2}(\tau_q) \right|^2. \quad (\text{F.21})$$

For the benchmark mass used in the main text, $M_{G_H} = 2.5 \text{ TeV}$, the dominant contribution generally comes from the top-quark loop if the coefficients η_q are flavor-hierarchical in the usual Yukawa sense. Nevertheless, because the process is loop-induced, the gg channel is naturally suppressed compared to the tree-level decay into quark–antiquark pairs whenever the latter is kinematically open.

G Appendix G: Justification of the cutoffs for vacuum–mismatch and thermal production in the $SU(3)_c$ transition

In this appendix we justify the different integration cutoffs used for the vacuum–mismatch and thermal channels in the $SU(3)_c \rightarrow U(2)$ benchmark of Secs. 7 and 8. As in the main text, the vacuum–mismatch contribution is terminated once the wall enters the terminal regime, while the thermal sector is evolved up to $\tau_{\text{final}} = 5\tau_{\text{term}}$. The reason is simple: the former is controlled by the proper acceleration $\alpha(\tau)$ (see equation (7.4)), whereas the latter is controlled by the accumulated heating of the shocked shell and therefore does not vanish merely because the acceleration becomes small.

Vacuum–mismatch production: exponential cutoff

The vacuum–mismatch channel is governed by the zero–mode occupancy, Eq. (7.6),

$$N_{k=0}(\tau) = \left[\frac{(\omega_+ + \omega_-)^2}{(\omega_+ - \omega_-)^2} \exp\left(\frac{4\omega_+}{\alpha(\tau)}\right) - 1 \right]^{-1}, \quad (\text{G.1})$$

which, for small positive $\alpha(\tau)$, reduces to

$$N_{k=0}(\tau) \simeq \left[\frac{(\omega_+ + \omega_-)^2}{(\omega_+ - \omega_-)^2} \right]^{-1} \exp\left(-\frac{4\omega_+}{\alpha(\tau)}\right). \quad (\text{G.2})$$

Thus the source is exponentially suppressed once the acceleration falls below the particle mass scale.

In the late-time regime we may approximate

$$\alpha(\tau) \simeq \alpha(0) e^{-\tau/\tau_{\text{term}}}, \quad (\text{G.3})$$

so that at $\tau = 5\tau_{\text{term}}$,

$$\alpha(5\tau_{\text{term}}) = \alpha(0) e^{-5} \simeq 1.07 \times 10^{-3} \text{ TeV}. \quad (\text{G.4})$$

For the scalar channel, $\omega_+ = \mu_s = 2.5 \text{ TeV}$, giving

$$\frac{4\mu_s}{\alpha(5\tau_{\text{term}})} \simeq 9.29 \times 10^3, \quad N_{k=0}^{(s)}(5\tau_{\text{term}}) \sim e^{-9.29 \times 10^3} \ll 10^{-4000}. \quad (\text{G.5})$$

For the massive-gluon channel, $\omega_+ = \mu_g = 1.0 \text{ TeV}$, giving

$$\frac{4\mu_g}{\alpha(5\tau_{\text{term}})} \simeq 3.75 \times 10^3, \quad N_{k=0}^{(g)}(5\tau_{\text{term}}) \sim e^{-3.75 \times 10^3} \ll 10^{-1600}. \quad (\text{G.6})$$

Hence by $5\tau_{\text{term}}$ the vacuum–mismatch source is completely extinguished in both channels.

The corresponding integrated tail is

$$\Delta N_{k=0}^{(\text{int})}(5\tau_{\text{term}}) = \int_{\tau_{\text{term}}}^{5\tau_{\text{term}}} d\tau N_{k=0}(\tau) 4\pi R^2(\tau) \sinh y(\tau). \quad (\text{G.7})$$

For the most ultra–relativistic benchmark in Table 3, $\delta = 10^{-12}$, we have

$$\tau_{\text{term}} \simeq 1.487 \times 10^6 \text{ TeV}^{-1}, \quad R_{\text{fin}} \simeq 1.051 \times 10^{12} \text{ TeV}^{-1}. \quad (\text{G.8})$$

Even though $R^2(\tau) \sinh y(\tau)$ grows polynomially over $[\tau_{\text{term}}, 5\tau_{\text{term}}]$, this growth is negligible compared to the exponential suppression above. The late-time contribution is therefore completely irrelevant compared with the integrated vacuum–mismatch yields in Table 3, which lie in the range

$$N_{\text{tot}}^{(\text{int})} \sim 10^3 - 10^7 \quad (\text{scalar}), \quad N_{\text{tot}}^{(\text{int})} \sim 10^4 - 10^8 \quad (\text{massive gluons}). \quad (\text{G.9})$$

This justifies terminating the vacuum–mismatch channel once the wall reaches the terminal regime.

Thermal production: integration time sensitivity

The thermal channel behaves differently. Its rate depends on the heated shell behind the wall and has the schematic form

$$\frac{dN_i}{d\tau} \propto 4\pi R^2(\tau) \sinh y(\tau) n_i[T_i(\tau)], \quad n_i(T) \propto T^3, \quad i = s, g. \quad (\text{G.10})$$

Unlike the vacuum–mismatch source, this contribution does not require a nonzero proper acceleration. As long as the shell remains hot and the wall continues to sweep out volume, thermal production continues.

In the full simulation the drag coefficient evolves as

$$\eta(\tau) = g_{\text{eff}}^2 T_{\text{eff}}^4(\tau), \quad (\text{G.11})$$

with $\eta(0)$ fixed by the terminal condition. Thus $\tau_{\text{term}} = \sigma/\eta(0)$ should be viewed as a convenient normalization scale inherited from the constant- η limit, rather than as an exact stopping time of the nonlinear system. In that constant-friction limit the accumulated energy deficit approaches its asymptotic value roughly as $1 - e^{-\tau/\tau_{\text{term}}}$, so evolving to

$$\tau_{\text{final}} = 5\tau_{\text{term}} \quad (\text{G.12})$$

already captures

$$1 - e^{-5} \simeq 0.993 \quad (\text{G.13})$$

of the asymptotic deficit. In the actual dynamic- η evolution the drag typically grows as the shocked layer heats up, so the approach to the quasi-terminal regime is at least as fast.

For the three terminal-velocity deficits used in the main text,

$$\delta = 10^{-12}, \quad 10^{-11}, \quad 10^{-10}, \quad (\text{G.14})$$

the corresponding values of $\tau_{\text{final}} = 5\tau_{\text{term}}$, taken from Table 4, are

$$\tau_{\text{final}} = 7.43 \times 10^6, \quad 2.35 \times 10^6, \quad 7.43 \times 10^5 \text{ TeV}^{-1}, \quad (\text{G.15})$$

respectively. Numerically we find that this choice already captures the dominant thermal yield: extending the evolution further changes the final multiplicities only at the few-percent level, while stopping significantly earlier would underestimate the result.

We therefore use $\tau_{\text{final}} = 5\tau_{\text{term}}$ as a conservative and numerically stable upper cutoff for the thermal sector. Beyond this point one expects additional effects—such as radiation reaction, scattering losses, and more detailed hydrodynamic backreaction of the shocked shell—to become important, while the gain in thermal multiplicity is already mild within the present framework.

H Appendix H: Proper Acceleration of the Bubble Wall

We derive here the magnitude of the proper acceleration of the bubble wall described by the equation $r^2 - t^2 = R_0^2$.

The bubble wall follows a hyperbolic trajectory in (t, r) spacetime, which can be parametrized using proper time τ (the time experienced by an observer on the bubble wall). The proper parametrization is:

$$t = R_0 \sinh\left(\frac{\tau}{R_0}\right), \quad r = R_0 \cosh\left(\frac{\tau}{R_0}\right). \quad (\text{H.1})$$

This satisfies the equation $r^2 - t^2 = R_0^2$, as:

$$R_0^2 \cosh^2\left(\frac{\tau}{R_0}\right) - R_0^2 \sinh^2\left(\frac{\tau}{R_0}\right) = R_0^2. \quad (\text{H.2})$$

The 4-velocity u^μ of the bubble wall is the derivative of the coordinates with respect to proper time

$$u^\mu = \left(\frac{dt}{d\tau}, \frac{dr}{d\tau}\right) = \left(\cosh\left(\frac{\tau}{R_0}\right), \sinh\left(\frac{\tau}{R_0}\right)\right). \quad (\text{H.3})$$

Thus, the norm of the 4-velocity is

$$u^\mu u_\mu = \left(\frac{dt}{d\tau}\right)^2 - \left(\frac{dr}{d\tau}\right)^2 = \cosh^2\left(\frac{\tau}{R_0}\right) - \sinh^2\left(\frac{\tau}{R_0}\right) = 1, \quad (\text{H.4})$$

confirming that τ is the proper time.

The 4-acceleration a^μ is the derivative of the 4-velocity with respect to proper time

$$a^\mu = \frac{du^\mu}{d\tau} = \left(\frac{1}{R_0} \sinh\left(\frac{\tau}{R_0}\right), \frac{1}{R_0} \cosh\left(\frac{\tau}{R_0}\right)\right). \quad (\text{H.5})$$

The norm of the 4-acceleration (which gives the proper acceleration) is

$$a^\mu a_\mu = \left(\frac{1}{R_0} \sinh\left(\frac{\tau}{R_0}\right)\right)^2 - \left(\frac{1}{R_0} \cosh\left(\frac{\tau}{R_0}\right)\right)^2 = -\frac{1}{R_0^2}. \quad (\text{H.6})$$

The magnitude of the proper acceleration is the absolute value of the norm [104, 105]

$$|a| = \sqrt{|a^\mu a_\mu|} = \frac{1}{R_0}. \quad (\text{H.7})$$

Thus, in the absence of friction, the magnitude of the proper acceleration of the bubble wall is constant and given by

$$\frac{1}{R_0}. \quad (\text{H.8})$$

I Appendix I: Numerical procedure

We evolve the coupled system $\{y(\tau), t(\tau), R(\tau), N_{\text{tot}}(\tau)\}$ defined by (7.3)–(7.7) using a fourth-order Runge–Kutta (RK4) method with adaptive steps. The state is initialized at nucleation by

$$y(0) = 0 \quad (v = 0), \quad t(0) = 0, \quad R(0) = R_0, \quad N_{\text{tot}}(0) = 0. \quad (\text{I.1})$$

At each substep we compute the instantaneous acceleration

$$\alpha_{\text{raw}}(\tau) = A - \frac{2}{R(\tau)} - B \sinh y(\tau). \quad (\text{I.2})$$

If $\alpha_{\text{raw}} \leq 0$, we enforce terminal balance by freezing $dy/d\tau = 0$ and setting $N_{k=0} = 0$; otherwise the system evolves as

$$\frac{dy}{d\tau} = \alpha_{\text{raw}}, \quad \frac{dt}{d\tau} = \cosh y, \quad \frac{dR}{d\tau} = \sinh y, \quad (\text{I.3})$$

with particle production

$$\frac{dN_{\text{tot}}}{d\tau} = N_{k=0}(\tau) 4\pi R(\tau)^2 \sinh y(\tau), \quad (\text{I.4})$$

and the instantaneous occupancy

$$N_{k=0}(\tau) = \left[\frac{(\omega_+ + \omega_-)^2}{(\omega_+ - \omega_-)^2} e^{\frac{4\mu}{\alpha_{\text{raw}}}} - 1 \right]^{-1}. \quad (\text{I.5})$$

Stability. For large arguments, specifically when $\frac{4\mu}{\alpha_{\text{raw}}} \gtrsim 200$, the stable asymptotic approximation is used:

$$N_{k=0}(\tau) \simeq \left[\frac{(\omega_+ + \omega_-)^2}{(\omega_+ - \omega_-)^2} \right]^{-1} e^{-4\mu/\alpha_{\text{raw}}}. \quad (\text{I.6})$$

The proper-time step is adapted according to the local drive,

$$d\tau \sim \frac{0.05}{\max(|\alpha_{\text{raw}}|, 10^{-6})}, \quad (\text{I.7})$$

and clamped to $20 \leq d\tau \leq 800$, ensuring stability both in the curvature-dominated early phase and in the slow terminal approach.

Stopping and checks. Integration halts when $\tau = \tau_{\text{term}}$. Convergence is checked by halving the initial $d\tau$ and demanding relative differences $< 10^{-4}$ in $\{\tau_{\text{term}}, R_{\text{fin}}, N_{\text{tot}}^{(\text{int})}\}$. Diagnostics include verifying

$$\frac{d\alpha}{d\tau} \leq -B\alpha, \quad \alpha(\tau) \leq \alpha(0)e^{-B\tau}, \quad (\text{I.8})$$

the monotonic growth of $R(\tau)$, and $N_{k=0} = 0$ whenever $\alpha_{\text{raw}} \leq 0$. To illustrate this, we study ultra-relativistic terminal deficits $\delta = 1 - v_{\text{term}}$, each mapped to a friction pair $(\eta, \tau_{\text{term}})$ fixing $B = \eta/\sigma$. The self-consistent balance is enforced by

$$\gamma_{\text{term}} v_{\text{term}} = \frac{\Delta V}{\eta}, \quad (\text{I.9})$$

so that for each δ ,

$$\eta(\delta) = \frac{\Delta V}{\gamma_{\text{term}} v_{\text{term}}}, \quad \tau_{\text{term}} = \frac{\sigma}{\eta}. \quad (\text{I.10})$$

This ensures the chosen terminal velocity matches the proper-time dynamics of the $\text{SU}(3)_c$ bubble wall.

References

- [1] D. Stojkovic, G.D. Starkman and R. Matsuo, *Dark energy, the colored anti-de Sitter vacuum, and LHC phenomenology*, *Phys. Rev. D* **77** (2008) 063006 [[hep-ph/0703246](#)].
- [2] K.S. Viswanathan and J.H. Yee, *First-order phase transitions in gauge theories*, *Phys. Rev. D* **19** (1979) 1906.
- [3] S.R. Coleman, *The Fate of the False Vacuum. 1. Semiclassical Theory*, *Phys. Rev. D* **15** (1977) 2929.
- [4] D.-C. Dai, R. Gregory and D. Stojkovic, *Connecting the Higgs Potential and Primordial Black Holes*, *Phys. Rev. D* **101** (2020) 125012 [[1909.00773](#)].
- [5] A. Sengupta, D. Stojkovic and D.-C. Dai, *The Signals of the Doomsday*, [2501.15848](#).
- [6] K. Yamamoto, T. Tanaka and M. Sasaki, *Particle spectrum created through bubble nucleation and quantum field theory in the Milne Universe*, *Phys. Rev. D* **51** (1995) 2968 [[gr-qc/9412011](#)].
- [7] L. Mersini-Houghton, *Relation between tunneling and particle production in vacuum decay*, *Phys. Rev. D* **59** (1999) 123521 [[hep-th/9902127](#)].
- [8] L. Mersini-Houghton, *Relation between tunneling and particle production in vacuum decay*, *Phys. Rev. D* **59** (1999) 123521 [[hep-th/9902127](#)].
- [9] M. Maziashvili, *Proper fluctuations associated with quantum tunneling in field theory*, *Mod. Phys. Lett. A* **18** (2003) 1895 [[hep-th/0302095](#)].
- [10] J.R. Espinosa and T. Konstandin, *An exploration of vacuum-decay valleys*, *JCAP* **01** (2026) 063 [[2506.06154](#)].
- [11] G. Isidori, G. Ridolfi and A. Strumia, *On the metastability of the standard model vacuum*, *Nucl. Phys. B* **609** (2001) 387 [[hep-ph/0104016](#)].
- [12] G. Hiller, T. Höhne, D.F. Litim and T. Steudtner, *Vacuum stability in the Standard Model and beyond*, *Phys. Rev. D* **110** (2024) 115017 [[2401.08811](#)].
- [13] J.R. Espinosa and T. Konstandin, *Exact tunneling solutions in multi-field potentials*, *JCAP* **03** (2024) 007 [[2312.12360](#)].
- [14] J.R. Espinosa, M. Garny, T. Konstandin and A. Riotto, *Gauge-Independent Scales Related to the Standard Model Vacuum Instability*, *Phys. Rev. D* **95** (2017) 056004 [[1608.06765](#)].
- [15] R. Alonso, J.C. Criado, R. Houtz and M. West, *Walls, bubbles and doom — the cosmology of HEFT*, *JHEP* **05** (2024) 049 [[2312.00881](#)].
- [16] M. Maziashvili, *Particle production by the expanding thin walled bubble*, *Mod. Phys. Lett. A* **19** (2004) 1391 [[hep-th/0311263](#)].
- [17] M. Maziashvili, *Particle production related to the tunneling in false vacuum decay*, *Mod. Phys. Lett. A* **18** (2003) 993 [[hep-th/0302062](#)].
- [18] T. Vachaspati and A. Vilenkin, *Quantum state of a nucleating bubble*, *Phys. Rev. D* **43** (1991) 3846.
- [19] M.S. Swanson, *Radiation from initially static vacuum structures*, *Phys. Rev. D* **32** (1985) 920.
- [20] T. Hamazaki, M. Sasaki, T. Tanaka and K. Yamamoto, *Selfexcitation of the tunneling scalar field in false vacuum decay*, *Phys. Rev. D* **53** (1996) 2045 [[gr-qc/9507006](#)].

- [21] M. Maziashvili, *Particle production by the thick walled bubble*, *Mod. Phys. Lett. A* **19** (2004) 671 [[hep-th/0311232](#)].
- [22] I.Y. Kobzarev, L.B. Okun and M.B. Voloshin, *Bubbles in Metastable Vacuum*, *Yad. Fiz.* **20** (1974) 1229.
- [23] C.J. Hogan, *NUCLEATION OF COSMOLOGICAL PHASE TRANSITIONS*, *Phys. Lett. B* **133** (1983) 172.
- [24] M. Kamionkowski, A. Kosowsky and M.S. Turner, *Gravitational radiation from first order phase transitions*, *Phys. Rev. D* **49** (1994) 2837 [[astro-ph/9310044](#)].
- [25] M.J. Baker, M. Breitbach, J. Kopp and L. Mittnacht, *Primordial black holes from first-order cosmological phase transitions*, *Phys. Lett. B* **868** (2025) 139625 [[2105.07481](#)].
- [26] M.J. Baker, M. Breitbach, J. Kopp and L. Mittnacht, *Detailed calculation of primordial black hole formation during first-order cosmological phase transitions*, *Phys. Rev. D* **111** (2025) 063544 [[2110.00005](#)].
- [27] E. Witten, *Cosmic Separation of Phases*, *Phys. Rev. D* **30** (1984) 272.
- [28] B. Shakya, *Aspects of particle production from bubble dynamics at a first order phase transition*, *Phys. Rev. D* **111** (2025) 023521 [[2308.16224](#)].
- [29] E.W. Kolb, S. Ling, A.J. Long and R.A. Rosen, *Cosmological gravitational particle production of massive spin-2 particles*, *JHEP* **05** (2023) 181 [[2302.04390](#)].
- [30] E.W. Kolb and A.J. Long, *Cosmological gravitational particle production and its implications for cosmological relics*, *Rev. Mod. Phys.* **96** (2024) 045005 [[2312.09042](#)].
- [31] J. Garcia-Bellido and E. Ruiz Morales, *Particle production from symmetry breaking after inflation*, *Phys. Lett. B* **536** (2002) 193 [[hep-ph/0109230](#)].
- [32] J.R. Espinosa, G.F. Giudice, E. Morgante, A. Riotto, L. Senatore, A. Strumia et al., *The cosmological Higgstory of the vacuum instability*, *JHEP* **09** (2015) 174 [[1505.04825](#)].
- [33] A.D. Linde, *Decay of the False Vacuum at Finite Temperature*, *Nucl. Phys. B* **216** (1983) 421.
- [34] M. Dine, R.G. Leigh, P.Y. Huet, A.D. Linde and D.A. Linde, *Towards the theory of the electroweak phase transition*, *Phys. Rev. D* **46** (1992) 550 [[hep-ph/9203203](#)].
- [35] A.D. Linde, *Fate of the False Vacuum at Finite Temperature: Theory and Applications*, *Phys. Lett. B* **100** (1981) 37.
- [36] A.D. Linde, *On the Vacuum Instability and the Higgs Meson Mass*, *Phys. Lett. B* **70** (1977) 306.
- [37] M. Dine, R.G. Leigh, P. Huet, A.D. Linde and D.A. Linde, *Comments on the electroweak phase transition*, *Phys. Lett. B* **283** (1992) 319 [[hep-ph/9203201](#)].
- [38] R. Kallosh and A.D. Linde, *Dark energy and the fate of the universe*, *JCAP* **02** (2003) 002 [[astro-ph/0301087](#)].
- [39] R. Kallosh, J. Kratochvil, A.D. Linde, E.V. Linder and M. Shmakova, *Observational bounds on cosmic doomsday*, *JCAP* **10** (2003) 015 [[astro-ph/0307185](#)].
- [40] I.V. Krive and A.D. Linde, *On the Vacuum Stability Problem in Gauge Theories*, *Nucl. Phys. B* **117** (1976) 265.
- [41] E. Bentivegna, V. Branchina, F. Contino and D. Zappalà, *Impact of New Physics on the EW vacuum stability in a curved spacetime background*, *JHEP* **12** (2017) 100 [[1708.01138](#)].

- [42] K. Kawana, P. Lu and K.-P. Xie, *First-order phase transition and fate of false vacuum remnants*, *JCAP* **10** (2022) 030 [[2206.09923](#)].
- [43] G. Degrandi, S.D. Vita, J. Elias-Miro, J.R. Espinosa, G.F. Giudice, G. Isidori et al., *Higgs mass and vacuum stability in the standard model at nnlo*, *JHEP* **1208** (2012) 098 [[1205.6497](#)].
- [44] M.S. Turner, E.J. Weinberg and L.M. Widrow, *Bubble nucleation in first order inflation and other cosmological phase transitions*, *Phys. Rev. D* **46** (1992) 2384.
- [45] M. Quiros, *Finite temperature field theory and phase transitions*, *Helv. Phys. Acta* **67** (1994) 451.
- [46] P.J. Steinhardt, *Relativistic Detonation Waves and Bubble Growth in False Vacuum Decay*, *Phys. Rev. D* **25** (1982) 2074.
- [47] J.R. Espinosa, T. Konstandin, J.M. No and G. Servant, *Energy Budget of Cosmological First-order Phase Transitions*, *JCAP* **06** (2010) 028 [[1004.4187](#) [[hep-ph](#)]].
- [48] W.-Y. Ai, J. Alexandre and S. Sarkar, *False vacuum decay rates, more precisely*, *Phys. Rev. D* **109** (2024) 045010 [[2312.04482](#)].
- [49] T. Tanaka, M. Sasaki and K. Yamamoto, *Field theoretic description of quantum fluctuations in multidimensional tunneling approach*, *Phys. Rev. D* **49** (1994) 1039.
- [50] CMS Collaboration, *Search for standard model production of four top quarks in proton-proton collisions at $\sqrt{s} = 13$ tev*, *Phys. Rev. D* **107** (2023) 092002 [[2303.03864](#)].
- [51] ATLAS Collaboration, *Search for pair-produced resonances in a four-jet final state in proton-proton collisions at $\sqrt{s} = 13$ tev with the atlas detector*, *Eur. Phys. J. C* **78** (2018) 250 [[1710.07171](#)].
- [52] G. Cacciapaglia, A. Deandrea, T. Flacke and A.M. Iyer, *Gluon-Photon Signatures for color octet at the LHC (and beyond)*, *JHEP* **05** (2020) 027 [[2002.01474](#)].
- [53] N. Vignaroli, *A New Strategy to Discover Heavy Colored Vectors at the Early LHC*, *Nuovo Cim. C* **034N6** (2011) 213 [[1107.4558](#)].
- [54] N. Vignaroli, *Phenomenology of heavy fermion and vector resonances in composite Higgs models*, Ph.D. thesis, Rome U., 2011. [1112.0218](#).
- [55] N. Vignaroli, *Z-peaked excess from heavy gluon decays to vectorlike quarks*, *Phys. Rev. D* **91** (2015) 115009 [[1504.01768](#)].
- [56] C. Bini, R. Contino and N. Vignaroli, *Heavy-light decay topologies as a new strategy to discover a heavy gluon*, *JHEP* **01** (2012) 157 [[1110.6058](#)].
- [57] E.G.S. Luna, *Diffraction phenomenology with massive gluons: Some recent developments*, *AIP Conf. Proc.* **1296** (2010) 183 [[1103.2334](#)].
- [58] R. Barcelo, A. Carmona, M. Chala, M. Masip and J. Santiago, *Single Vectorlike Quark Production at the LHC*, *Nucl. Phys. B* **857** (2012) 172 [[1110.5914](#)].
- [59] C. Bierlich et al., *A comprehensive guide to the physics and usage of PYTHIA 8.3*, *SciPost Phys. Codeb.* **2022** (2022) 8 [[2203.11601](#)].
- [60] T. Sjöstrand, S. Ask, J.R. Christiansen, R. Corke, N. Desai, P. Ilten et al., *An introduction to PYTHIA 8.2*, *Comput. Phys. Commun.* **191** (2015) 159 [[1410.3012](#)].

- [61] M.I. Gresham and M.B. Wise, *Color octet scalar production at the LHC*, *Phys. Rev. D* **76** (2007) 075003 [[0706.0909](#)].
- [62] M. Gerbush, T.J. Khoo, D.J. Phalen, A. Pierce and D. Tucker-Smith, *Color-octet scalars at the CERN LHC*, *Phys. Rev. D* **77** (2008) 095003 [[0710.3133](#)].
- [63] A. Djouadi, *Higgs Physics: Theory*, *Pramana* **79** (2012) 513 [[1203.4199](#)].
- [64] H.E. Logan, *TASI 2013 lectures on Higgs physics within and beyond the Standard Model*, [1406.1786](#).
- [65] R.S. Chivukula, E.H. Simmons and N. Vignaroli, *Same-Sign Dileptons from Colored Scalars in the Flavorful Top-Coloron Model*, *Phys. Rev. D* **88** (2013) 034006 [[1306.2248](#)].
- [66] R. Sekhar Chivukula, E.H. Simmons and N. Vignaroli, *Distinguishing dijet resonances at the LHC*, *Phys. Rev. D* **91** (2015) 055019 [[1412.3094](#)].
- [67] R.S. Chivukula, A. Farzinia and E.H. Simmons, *Vacuum Stability and Triviality Analyses of the Renormalizable Coloron Model*, *Phys. Rev. D* **92** (2015) 055002 [[1504.03012](#)].
- [68] E. Drueke, J. Nutter, R. Schwienhorst, N. Vignaroli, D.G.E. Walker and J.-H. Yu, *Single Top Production as a Probe of Heavy Resonances*, *Phys. Rev. D* **91** (2015) 054020 [[1409.7607](#)].
- [69] B.A. Dobrescu, K. Kong and R. Mahbubani, *Massive color-octet bosons and pairs of resonances at hadron colliders*, *Phys. Lett. B* **670** (2008) 119 [[0709.2378](#)].
- [70] E.H. Simmons, *Coloron phenomenology*, *Phys. Rev. D* **55** (1997) 1678 [[hep-ph/9608269](#)].
- [71] E.H. Simmons, *Colorons: Theory and phenomenology*, in *International Workshop on Perspectives of Strong Coupling Gauge Theories (SCGT 96)*, pp. 100–106, 11, 1996 [[hep-ph/9701282](#)].
- [72] P.H. Frampton and S.L. Glashow, *Chiral Color: An Alternative to the Standard Model*, *Phys. Lett. B* **190** (1987) 157.
- [73] A. Davidson and K.C. Wali, *BARYON NUMBER VIOLATION BY CHIRAL COLOR AXINSTANTONS*, *Phys. Lett. B* **194** (1987) 247.
- [74] P. Fileviez Perez, R. Gavin, T. McElmurry and F. Petriello, *Grand Unification and Light Color-Octet Scalars at the LHC*, *Phys. Rev. D* **78** (2008) 115017 [[0809.2106](#)].
- [75] S. Schumann, A. Renaud and D. Zerwas, *Hadronically decaying color-adjoint scalars at the LHC*, *JHEP* **09** (2011) 074 [[1108.2957](#)].
- [76] X.-G. He, H. Phoon, Y. Tang and G. Valencia, *Unitarity and vacuum stability constraints on the couplings of color octet scalars*, *JHEP* **05** (2013) 026 [[1303.4848](#)].
- [77] J.M. Arnold and B. Fornal, *Color octet scalars and high p_T four-jet events at LHC*, *Phys. Rev. D* **85** (2012) 055020 [[1112.0003](#)].
- [78] A. Hayreter and G. Valencia, *LHC constraints on color octet scalars*, *Phys. Rev. D* **96** (2017) 035004 [[1703.04164](#)].
- [79] V. Miralles and A. Pich, *LHC bounds on colored scalars*, *Phys. Rev. D* **100** (2019) 115042 [[1910.07947](#)].
- [80] A. Idilbi, C. Kim and T. Mehen, *Pair Production of Color-Octet Scalars at the LHC*, *Phys. Rev. D* **82** (2010) 075017 [[1007.0865](#)].
- [81] C. Kim and T. Mehen, *Color Octet Scalar Bound States at the LHC*, *Phys. Rev. D* **79** (2009) 035011 [[0812.0307](#)].

- [82] J. Sayre, D.A. Dicus, C. Kao and S. Nandi, *Searching for Colorons at the Large Hadron Collider*, *Phys. Rev. D* **84** (2011) 015011 [[1105.3219](#)].
- [83] A. Hayreter and G. Valencia, *Color-octet scalar decays to a gluon and an electroweak gauge boson in the Manohar-Wise model*, *Phys. Rev. D* **102** (2020) 115033 [[1810.04048](#)].
- [84] N.V. Krasnikov, *The Phenomenology of scalar color octets*, *JETP Lett.* **62** (1995) 7 [[hep-ph/9506431](#)].
- [85] E. Eichten and C. Quigg, *Mesons with beauty and charm: Spectroscopy*, *Phys. Rev. D* **17** (1978) 3090.
- [86] N. Brambilla, S. Eidelman, B. Heltsley et al., *Heavy quarkonium: Progress, puzzles, and opportunities*, *Phys. Rept.* **500** (2011) 1.
- [87] T. Appelquist and J. Carazzone, *Infrared Singularities and Massive Fields*, *Phys. Rev. D* **11** (1975) 2856.
- [88] Y.P. Goncharov, *Quark confinement mechanism and the scale Λ_{QCD}* , *Int. J. Theor. Phys.* **51** (2012) 428 [[1201.4327](#)].
- [89] Z. Si, H. Wang, L. Wang, Y. Xiao and Y. Zhang, *The bubble wall velocity in local thermal equilibrium and energy budget with full effective potential*, *JHEP* **09** (2025) 029 [[2505.19584](#)].
- [90] G.D. Moore, *Electroweak bubble wall friction: analytic results*, *Journal of High Energy Physics* **2000** (2000) 006–006.
- [91] G.D. Moore and T. Prokopec, *Bubble wall velocity in a first order electroweak phase transition*, *Phys. Rev. Lett.* **75** (1995) 777 [[hep-ph/9503296](#)].
- [92] C. Branchina, A. Conaci, S. De Curtis and L. Delle Rose, *Electroweak Phase Transition and Bubble Wall Velocity in Local Thermal Equilibrium*, [2504.21213](#).
- [93] D. Bodeker and G.D. Moore, *Electroweak Bubble Wall Speed Limit*, *JCAP* **05** (2017) 025 [[1703.08215](#)].
- [94] A. Azatov and M. Vanvlasselaer, *Bubble wall velocity: heavy physics effects*, *JCAP* **01** (2021) 058 [[2010.02590](#)].
- [95] A. Azatov, G. Barni, R. Petrossian-Byrne and M. Vanvlasselaer, *Quantisation across bubble walls and friction*, *JHEP* **05** (2024) 294 [[2310.06972](#)].
- [96] W.-Y. Ai, M. Carosi, B. Garbrecht, C. Tamarit and M. Vanvlasselaer, *Bubble wall dynamics from nonequilibrium quantum field theory*, *JHEP* **08** (2025) 077 [[2504.13725](#)].
- [97] L. Giombi and M. Hindmarsh, *General relativistic bubble growth in cosmological phase transitions*, *JCAP* **03** (2024) 059 [[2307.12080](#)].
- [98] R.-G. Cai and S.-J. Wang, *Effective picture of bubble expansion*, *JCAP* **03** (2021) 096 [[2011.11451](#)].
- [99] S. Balaji, M. Spannowsky and C. Tamarit, *Cosmological bubble friction in local equilibrium*, *JCAP* **03** (2021) 051 [[2010.08013](#)].
- [100] W.-Y. Ai, B. Garbrecht and C. Tamarit, *Bubble wall velocities in local equilibrium*, *JCAP* **03** (2022) 015 [[2109.13710](#)].
- [101] W.-Y. Ai, B. Laurent and J. van de Vis, *Model-independent bubble wall velocities in local thermal equilibrium*, *JCAP* **07** (2023) 002 [[2303.10171](#)].

- [102] S. Höche, J. Kozaczuk, A.J. Long, J. Turner and Y. Wang, *Towards an all-orders calculation of the electroweak bubble wall velocity*, *JCAP* **03** (2021) 009 [[2007.10343](#)].
- [103] A.J. Long and J. Turner, *Thermal pressure on ultrarelativistic bubbles from a semiclassical formalism*, *JCAP* **11** (2024) 024 [[2407.18196](#)].
- [104] W.R. Walker, *Particle and Energy Creation by Moving Mirrors*, *Phys. Rev. D* **31** (1985) 767.
- [105] M.R.R. Good, P.R. Anderson and C.R. Evans, *Time Dependence of Particle Creation from Accelerating Mirrors*, *Phys. Rev. D* **88** (2013) 025023 [[1303.6756](#)].